MODELLING THE THREE-DIMENSIONAL TIDAL FLOW STRUCTURE IN SEMI-ENCLOSED BASINS

Olav van Duin

UNIVERSITEIT TWENTE.

MODELLING THE THREE-DIMENSIONAL TIDAL FLOW STRUCTURE IN SEMI-ENCLOSED BASINS

This Master thesis was written by:
Olav J.M. van Duin

as the thesis for a Master's degree in:
Water Engineering & Management, University of Twente

under the supervision of the following committee:

Supervisor:	Prof. Dr. Suzanne J.M.H. Hulscher (University of Twente)
Daily supervisor:	Dr. Ir. Pieter C. Roos (University of Twente)
External supervisor:	Dr. Henk M. Schuttelaars (TU Delft)

ABSTRACT

Coastal areas are generally intensely used areas with high population density and economic activity. On a basin scale the tide directly determines water levels and currents in a basin. These flow characteristics furthermore determine the shape of the basin itself, for example the forming and evolution of tidal sandbanks, which in turn influences the flow pattern. Because of its importance for various human and natural activities the modelling of tidal flow has been studied by many authors in the past. This has lead to depth-averaged (2DH) and 3D models amongst others

The first analytical 3D-model that describes tidal flow in a semi-enclosed basin using Kelvin and Poincaré modes with partial slip was created for this research. For this the method devised by Mofjeld (1980) for 3D tidal flow along a single coast with viscosity and no-slip was extended, thereby following Taylor's approach (1921).

As a reference situation the Northern Part of the North Sea was modeled and the properties of the Kelvin and Poincaré modes described. Also the flow and shear stress properties were studied. The flow properties were also compared to an equivalent 2DH model but for this first values for the friction parameter had to be determined. For this various methods were adopted with varying success in approximating the 3D properties. It is clear that that 3D structure is important to be able to precisely determine the flow properties. The value for the friction parameter that gives the best results of the methods employed was that be found by fitting the Kelvin dissipation factor of the 3D model (using viscosity and slip parameters) with the 2DH model (using a friction parameter).

The fitting of the Kelvin dissipation factor lead to a friction parameter of $1.7*10^{-3}$ m/s for the reference case (the 3D model had a slip parameter of 0.005 m/s and a viscosity parameter of 0.09 m^2/s). With this parameter the 2DH model results were compared with the 3D model results, showing that 3D structure is indeed important. Eventually this friction lead to an average error in predicting 3D longitudinal bottom shear stress amplitude with a 2DH model of 13% while the theoretically best result would have been 3%.

This all leads to the conclusion that continued research in this area can further improve 3D and 2DH modeling.

FOREWORD

This thesis was written as the culmination of my Master study Water Engineering & Management at the University of Twente. An important aspect of this study is relating the technical knowledge gained to practical and societal needs. Though this research was rather mathematical, it still had a solid practical context which helped in making the research itself understandable, useful and more pleasurable.

A second very important part during my research was the guidance of my supervisors, Suzanne, Henk and Pieter. Their insight and years of experience regarding the handled subjects was invaluable in bringing this research to a good end and making it scientifically and practically valid. Though I have to admit it was sometimes boggling to hear them discuss what lied behind things I handled lightly and didn't explain or explore in depth, all in all this meant that I learned much more than I would have done in solitude. So, thank you all! I would especially like to thank my daily supervisor Pieter, who was almost always available for guidance and answers.

By doing my research as a graduation intern at the University of Twente itself I had the opportunity to work with a group of other Master students in the room reserved for the graduation interns. This of course meant that there was enough to discuss, talk about and laugh during lunch breaks, coffee breaks, cake and coffee breaks, cookies and coffee breaks, et cetera. This was a welcome relief from the primarily individual undertaking the writing of a Master thesis is. The various activities that were organized/instigated like *wadwalking*, barbecues and even a think-tank-competition by certain individuals (Wiebe, Bert, Erwin, Frank, Daniël, I hope I'm not forgetting someone…) also greatly helped in making this an enjoyable time. Furthermore I would especially like to thank Wiebe for being my support in all things mathematical and tidal; it would have been lonely without you! But of course, all other fellow students also deserve praise for their support and good company!

And finally I thank all my friends and family for being there and thereby giving me a life besides my daily scientific endeavours. Most of all I thank Annick, for being an unexpected but dearly loved light in my life.

I hope you enjoy reading what I've written about three dimensional tidal flow structure in semi-enclosed basins!

Olav van Duin,

the 25th of September 2009, Enschede

CONTENTS AT A GLANCE

TABLE OF CONTENTS

1 INTRODUCTION

Coastal areas are generally intensely used areas with high population density and economic activity. This is partly because of the vicinity of the sea, which offers great opportunities for human development. But the sea does not only offer opportunities, it can also be a threat. On a basin scale tidal flow directly determines water levels and currents in a basin. These flow characteristics furthermore determine the shape of the basin itself, for example the formation and evolution of tidal sandbanks, which in turn influences the flow pattern.

It is important to understand flow properties in these areas for functions like ecology, safety and transport. This research focuses on a tidal flow in a specific marine environment, namely semi-enclosed basins with widths and lengths in the order of hundreds of kilometres and depths in the order of tens of meters. It is important to examine the 3D aspects of flow in these basins as they for example determine the near-bed flow which controls sediment transport (Prandle, 1997) and the formation of bed features like sand waves (Hulscher, 1996 and Gerkema, 2000). Differences in 3D flow properties can be significant in semi-enclosed basins, which is observed for instance in the Chignecto Bay (Tee, 1982). Furthermore the Long Island Sound – Block Island Sound channel shows tidally induced residual currents (Ianniello, 1981), which can have a large influence on net sediment transport. Besides the more general expected behaviour lateral flow circulations are expected for tidal flow which controls the dispersion of pollutants and salt water (Prandle, 1982 and Huijts et al., 2009).

In the ideal situation a fully 3D model is available that incorporates all physical processes and can be used to study flow in semi-enclosed basins. However, incorporating all these aspects requires a large amount of work and the resulting model would be rather complex and time-consuming to use. Also, because of the inherently complex nature of the mathematics associated with this type of flow the model would have to be numerical which makes it hard to exactly distinguish between the effects of different aspects and properties. To be able to study which processes are most important to incorporate, it is valuable to make (increasingly complex) analytical models which allow for an easier interpretation of the results. Such a model can be used to determine which processes are relevant in which situation and therefore which are most important to include in a numerical model. This study aims to produce a 3D analytical model that is a logical extension of the work done in the past. In the following paragraphs this will be explained in detail.

1.1 PROBLEM DESCRIPTION

Consider a shallow sea that is largely constrained on three sides by coasts. The tidal pattern in such a basin is affected by the three boundaries as well as driving forces. The tidal wave enters the basin from open deep sea and propagates between the two parallel coasts until it reaches the closed lateral boundary. Because of the presence of this boundary the tidal wave turns around and propagates back towards the open end. Because a Kelvin wave, a simple representation of a tidal wave, cannot make this turn an additional type of wave modes is needed to represent the flow near the lateral boundary. These additional modes are called Poincaré modes. In the figure below a very rough approximation of this tidal wave movement can be seen.

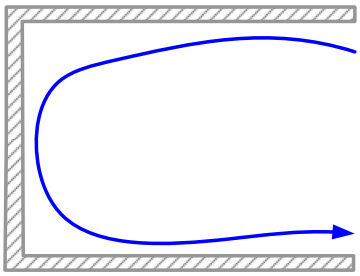

Figure 1: schematization of the tidal wave movement

If the basin is sufficiently large, Coriolis effects will occur. This fictitious force originates from the Earth's rotation, deflecting flow to the right on the Northern hemisphere. Due to continuity and the boundaries this deflection will cause circulation in the vertical. This and the fact that particles tend to corkscrew in and out of the basin (Winant, 2007) indicate that a depth-averaged (2DH) approach will lose important properties of the flow.

Furthermore vertical viscosity means that the tidal wave experiences dissipation while moving through the basin. In a depth-averaged model bed friction is a parameterization of this 3D-effect. A solid representation of the vertical pattern of currents is especially important for morphological studies where for instance the velocity derivatives at the bed are used for the calculation of bottom shear stress which in turn determines the morphological development of the sea bottom.

It is expected that a combination of an incoming and outgoing Kelvin wave and a truncated set of Poincaré modes can describe the tidal dynamics in a semi-enclosed basin sufficiently well to get a good idea of the processes at work and the consequences for bottom shear stress. In the following chapters the application of and the mentioned wave modes themselves will be explained in more detail.

1.2 RESEARCH CONTEXT

Because of its importance for various human and natural activities the modelling of tidal flow has been studied by many authors in the past. A quick overview will be given of the relevant studies which incorporate some of the processes that will be modelled in this study, though none of them individually contains *all* of these aspects.

The propagation of a tidal wave in a semi-enclosed basin is referred to as the 'Taylor problem'; this author investigated how a Kelvin wave is reflected in a rectangular semi-enclosed basin (Taylor, 1921). The analytical solution presented does not take dissipation into account and is depth-averaged. To model the closed lateral boundary Taylor found Poincaré modes to complement the incoming and outgoing Kelvin waves. Hendershott & Speranza (1971) expanded on Taylor's work by allowing the boundary at the head of the basin to absorb energy, thus introducing a mechanism for dissipation. Opposed to dissipation localized at the lateral boundary, dissipation throughout the basin was modelled by Rienecker & Teubner (1980) by introducing friction terms. Mofjeld (1980) examined 3D properties of tidal flow along a single straight coast with a flat bottom, incorporating Coriolis and vertical viscosity effects. For this the author used Kelvin waves to represent the tidal flow. Constant viscosity is assumed and a no-slip condition is applied at the bottom. Pedlosky (1982) presents a solution for the depth-averaged tidal flow in an infinite channel (a shallow stretch of sea with two parallel boundaries) which leads to Poincaré and Kelvin wave modes. The basin shape was studied in 2DH and a flat bottom was used. The author took Coriolis effects into account, but no bed friction (as a 2DH-representation of vertical viscosity). Davies & Jones (1995) also studied the basin shape that is studied for this research. They made a numerical model for a semi-enclosed basin with a sloping bottom as well as a flat bottom. The authors incorporated nonlinear terms (advection), non-constant viscosity and Coriolis effects. They were the only ones mentioned here that studied a partial-slip condition as well as a no-slip condition. Winant (2007) also looked at tidal flow in an *elongated* semi-enclosed basin, but for a bottom that is parabolic-shaped in the transverse. The author has explained the lateral flow circulations in a semi-enclosed basin with a 3D basin-model that incorporates Coriolis as well as vertical viscosity effects. However, this solution is only applicable to basins that are narrow and it is unclear whether this approach will work with a non-parabolic bottom.

This research strives to make the first analytical 3D-model that describes tidal flow in a semi-enclosed basin using Kelvin and Poincaré modes with partial slip. A drawback of this approach is that it can only be applied to flat bottoms, eddy viscosity is constant and that only linear terms are taken into account. On the plus side this model has no condition that the basin must be narrow like that of Winant (2007). Also, the chosen analytical approach with Kelvin and Poincaré modes makes that the

final model is easily understood and the influence of various parameters can be easily investigated. Furthermore the assumption of constant viscosity actually implies use of a partial slip condition to get realistic velocities and shear stresses (Hulscher, 1996 and Hulscher & Van den Brink, 2001), so use of this combination is more correct than the original work of Mofjeld (1980). The use of a partial slip condition allows for a relatively simple though effective calculation of bottom shear stress (Gerkema, 2000); it avoids solving the complex processes in the near-bottom boundary layer described in Bowden (1978).

1.3 RESEARCH QUESTIONS

The research questions that will be investigated in the following report are:

1. In what way can Mofjeld's (1980) analysis and the approach documented by Pedlosky (1982) be combined and extended to find Kelvin and Poincaré modes in an infinite channel of finite width as a solution to 3D tidal flow including a partial slip condition?
   - 1.a What are the typical properties of these wave modes?
   - 1.b Which values of the friction parameter in an equivalent depth-averaged model should be chosen to get the same properties given a certain combination of the viscosity and slip parameters?
   - 1.c How should these wave modes described above be combined to simulate tidal flow in a semi-enclosed basin (i.e. the Taylor problem)?
2. Using the combined wave modes; what are the 3D tidal flow properties (elevation, currents, bottom shear stresses) in the Northern part of the North Sea?
   - 2.a How do these properties differ in the vertical? And for varying slip parameter and vertical viscosity?
   - 2.b Using the friction parameters found before; how well does the depth-averaged model correspond to the 3D model concerning flow properties? Which method produces the best results?

1.4 APPROACH

In short the goal of this research is to set up a mathematical model to calculate the 3D flow field in a semi-enclosed basin, investigate its properties and see if an equivalent depth-averaged model can achieve similar results. The processes that are included are the pressure gradient, Coriolis force and eddy viscosity. A partial-slip condition will be applied at the sea bottom. The complete model setup is described in chapter 2.

The method applied by Mofjeld (1980) for tidal flow along a single coast is extended to an infinite channel (also following the method described by Pedlosky, 1982) and wave modes are sought that satisfy the boundary conditions and governing equations (see chapter 3). The depth-averaged versions of these modes are presented, as well as a numerical method which combines these wave modes in such a way that the condition at the closed lateral boundary is satisfied (see chapter 4). The properties of the wave modes and the quasi-analytical model which represents the tidal flow of a semi-enclosed basin are also examined and an attempt is made to fit an equivalent depth-averaged model to these properties (see chapter 5). The quasi-analytical model is used to predict the bottom shear stress and this is also compared to the equivalent depth-averaged model (see chapter 6). The final chapters handle the discussion, conclusion and recommendation. Appendices are included with additional information.

2 MODEL FORMULATION OF TIDAL FLOW IN A SEMI-ENCLOSED BASIN

In this chapter the setup of the model will be described. First an impression will be given of what basins are modelled. After that the governing equations and boundary conditions are derived from the full Navier-Stokes equations by making appropriate assumptions for the kind of basins described before. After that the equations are scaled and the linear versions are found.

2.1 DESCRIPTION OF THE MODELLED BASIN

The basin shape (see Figure 2) that will be used for this study is that of a semi-enclosed semi-infinite rectangular basin with width B*, and constant undisturbed water depth H*. It should be noted that there is no condition imposed on the dotted lines, it is just to signify that the basin extends infinitely beyond the dotted lines. The horizontal velocity parallel to the alongshore direction x* is called u*, the horizontal velocity parallel to the cross shore direction y* is called v* and the upward vertical velocity parallel to the vertical direction z* is called w*. The displacement of the water surface with respect to the undisturbed water depth is called η*, which depends on x*, y* and time t*. The origin of the coordinate system lies at the bottom of the basin in the lower left corner as shown in Figure 2.

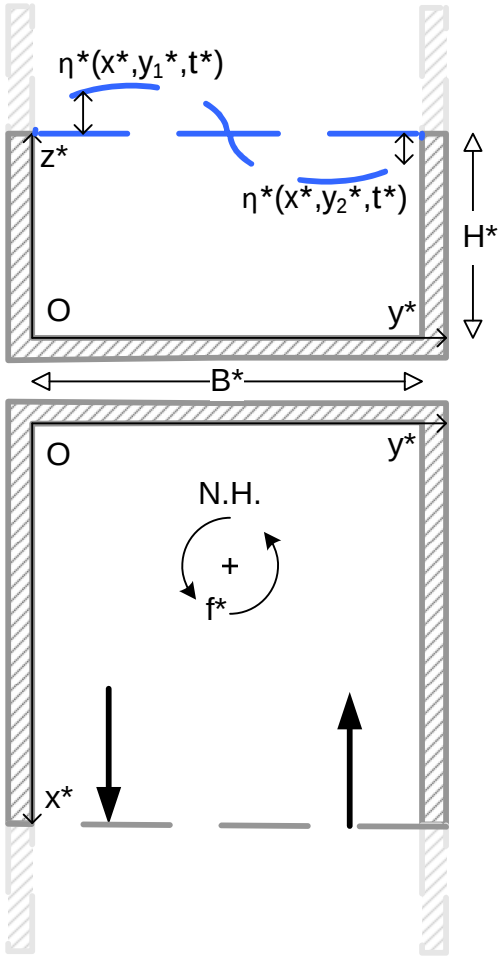

Figure 2: side view (top) and top view (bottom) of a semi-enclosed basin (not to scale)

This basin will be modelled on the f-plane (a local approximation of the spherical Earth) and lies on the Northern Hemisphere. The former implies that the Coriolis deflection is constant, while the latter implies that the tide will rotate counter-clockwise. The tidal flow enters the basin on the right side of

Figure 2 and exits on the left side; this basic tidal movement will be represented by an incoming and outgoing Kelvin wave. At the closed lateral boundary the tidal wave will have to turn, this will generate so-called Poincaré modes. The incoming Kelvin wave will be imposed while the other wave modes (the outgoing Kelvin wave and the Poincaré modes) will follow from the solution method. These modes have no depth-integrated normal flow through the longitudinal boundaries. The model will adjust the amplitudes of the possible modes to ensure there is no normal depth-averaged flow at the closed lateral boundary when the used modes are superimposed.

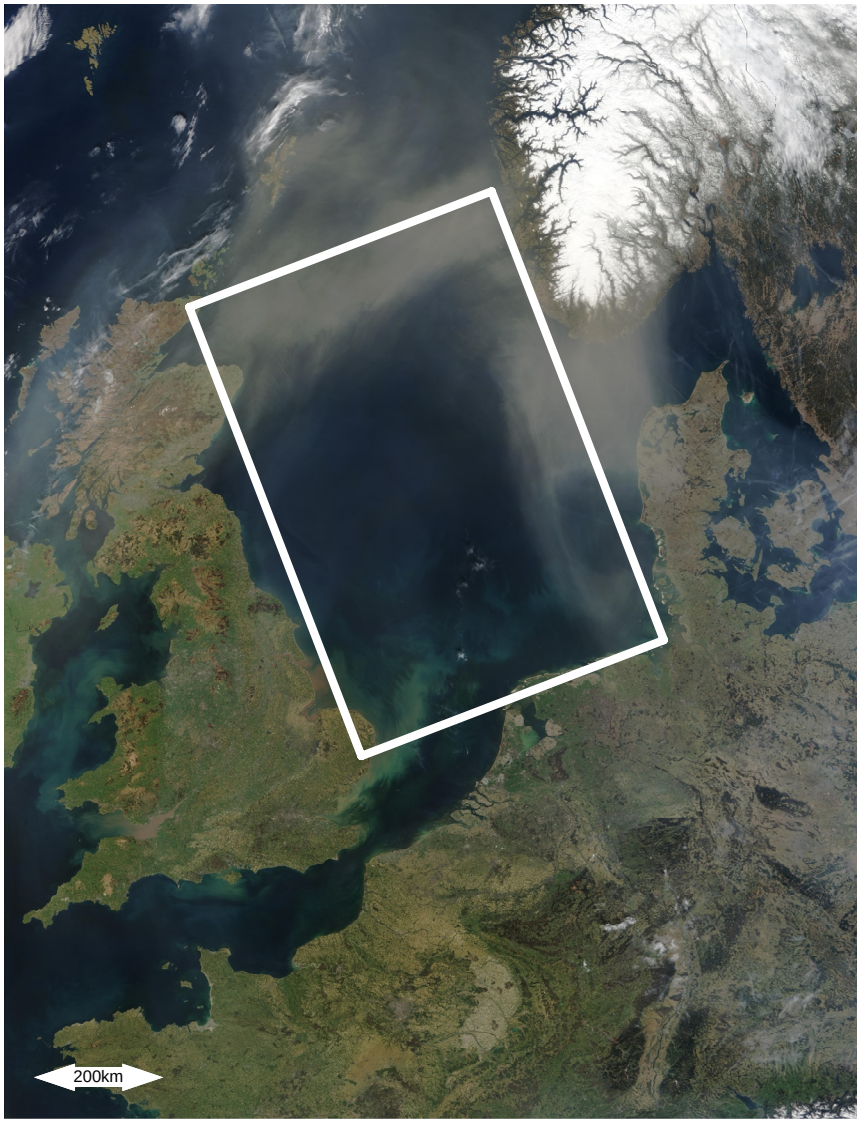

Figure 3: section of the North Sea that will be modeled (source: http://visibleearth.nasa.gov)

The model will be tailored to basins with a length and width in the hundreds of kilometres and a depth in the tens of meters. The latitude will be around 50 degrees and the modelled tidal constituent will be the M2-tide. Actual physical values are presented when the properties of the model are investigated as a reference case. Because the aim of this study is not to model a *specific* basin properly, the *exact* physical values are not relevant now. Later in this thesis the model will be applied to the Northern part of the North Sea, as can be seen in the figure above.

2.2 MODIFYING THE GOVERNING EQUATIONS AND BOUNDARY CONDITIONS

In this paragraph the governing equations and boundary conditions that will be used to describe tidal flow in a semi-enclosed basin are presented. The governing equations follow from the type of basin that will be modeled and the original full Navier-Stokes equations, see appendix A for details. In the following paragraph these equations and the boundary conditions will be scaled.

2.2.1 GOVERNING EQUATIONS

Under the conditions sketched in appendix A the momentum equations and the continuity equation are as follows. An asterisk denotes that the dimensional version of the parameter or variable is meant; in paragraph 2.3 the non-dimensional versions will be introduced.

$$u^*_{t^*} + u^* u^*_{x^*} + v^* u^*_{y^*} + w^* u^*_{z^*} - f^* v^* = -g^* h^*_{x^*} + A^*_v u^*_{z^* z^*} \qquad [2.1]$$

$$v^*_{t^*} + u^* v^*_{x^*} + v^* v^*_{y^*} + w^* v^*_{z^*} + f^* u^* = -g^* h^*_{y^*} + A^*_v v^*_{z^* z^*} \qquad [2.2]$$

$$u^*_{x^*} + v^*_{y^*} + w^*_{z^*} = 0 \qquad [2.3]$$

Here the parameter f* denotes the Coriolis parameter, A_v* vertical eddy viscosity and g* the gravity acceleration. The subscripts x*, y*, z*, t* denote the derivative of that variable to the respective coordinate.

2.2.2 BOUNDARY CONDITIONS

At the walls of the basin a condition is imposed that there can be no depth-integrated normal flow through the wall. A stronger condition would be that all flow is zero at the coast, this however means that the complex flow in the boundary layer at the coast needs to be resolved (Mofjeld, 1980). Mofjeld (1980) explains that this condition can be replaced by disregarding these side-layers and only considering the region seawards of those layers, this will therefore also be done here. It should be noted that the fact that by disregarding these horizontal side-layers horizontal viscosity is implicitly neglected (in appendix A horizontal viscosity was disregarded beforehand). From now on, when the coastal boundary conditions are mentioned actually *near-coastal* boundary conditions are meant.

$$\int_0^{H^*+h^*} v^* dz^* = 0 \quad \text{at} \qquad y^* = 0, B^* \qquad [2.4]$$

$$\int_0^{H^*+h^*} u^* dz^* = 0 \quad \text{at} \qquad x^* = 0 \qquad [2.5]$$

The condition at the parallel walls will be satisfied by the wave modes individually, while the condition at the lateral wall will be satisfied by the wave modes collectively (by use of a collocation method). At the free water surface a no-stress dynamic boundary condition and a kinematic boundary condition is applied. These conditions will be met by the wave modes individually. It should be noted that the upper expression is an approximation of the actual condition which uses the derivatives along the surface normal. Because of the assumption of long waves (surface elevation is small compared to tidal wave length), the surface normal points almost exactly upward (i.e. parallel to the vertical axis z*) and this approximation can be used.

$$\begin{cases} u^*_{z^*}, v^*_{z^*} = 0 \\ w^* = h^*_{t^*} + u^* h^*_{x^*} + v^* h^*_{y^*} \end{cases} \quad \text{at} \qquad z^* = H^* + h^* \qquad [2.6]$$

A dynamic boundary condition (partial slip, which approaches no slip when the stress parameter s* goes to infinity) is applied at the bed, as well as a kinematic boundary condition. These conditions will also be met by the wave modes individually. Using a partial slip condition makes the assumption of constant eddy viscosity reasonable (Hulscher, 1996). It should be noted that the partial slip condition actually uses the derivatives along the bottom normal, but because a flat bottom is used the bottom normal is parallel to the z*-axis, so this version can be used.

$$\begin{cases} A_v^* u_{z^*}^* = s^* u^* \\ A_v^* v_{z^*}^* = s^* v^* \qquad \text{at} \qquad z^* = 0 \\ w^* = 0 \end{cases} \qquad [2.7]$$

2.3 SCALING THE FLOW EQUATIONS AND BOUNDARY CONDITIONS

The dimensions and variables are scaled with certain scaling parameters which are typical values for the dimensions or variable they are applied to. By doing this the resulting dimensionless parameters are more relatable to the system and its flow properties than the original parameters were. Also, when the equations are scaled, the order of magnitude of the terms can be more easily compared thereby making it easier to see which are most significant. The expressions for the dimensionless parameters can be found below.

$$t = s^* t^* \quad [2.8] \qquad (x, y) = K^* (x^*, y^*) \quad [2.9] \qquad z = z^* / H^* \quad [2.10]$$

$$h = h^* / h_0^* \quad [2.11] \qquad (u, v) = (u^*, v^*) / U^* \quad [2.12] \qquad w = w^* / W^* \quad [2.13]$$

Here the tidal frequency s^*, tidal elevation amplitude h_0^*, maximum horizontal velocity $U^* = h_0^* \sqrt{g^* / H^*}$ [2.14], wave number $K^* = s^* / \sqrt{g^* H^*}$ [2.15] and the vertical velocity scale $W^* = K^* H^* U^* = s^* h_0^*$ [2.16] (this follows from applying the previous scaling parameters to the continuity equation [2.3]) are used. Both U* and K* are typical for inviscid 2D Kelvin waves (Pedlosky, 1982). W* is the maximum horizontal velocity adjusted for the relative difference in vertical and horizontal length scale. An additional interpretation is that W* is the amplitude divided by the tidal period. This all means that 1 unit of t equals the tidal period, 1 unit of x or y equals the Kelvin wave length divided by 2π, 1 unit of z equals the water depth, 1 unit of η equals the Kelvin elevation amplitude, 1 unit of u or v equals the Kelvin velocity amplitude and 1 unit of w equals the speed of going up with a speed of one amplitude per tidal cycle.

After substituting the scaled parameters new scaled versions of the original equations and boundary conditions are found. These are used to derive the linear system of equations in the following paragraph.

2.3.1 SCALED GOVERNING EQUATIONS

Introduction of the non-dimensional parameters and some rearranging yields the following for the equations of motion and the continuity equation.

$$u_t + e\left[u u_x + v u_y + w u_z\right] - fv = -h_x + \frac{d_v^2}{2} u_{zz} \qquad [2.17]$$

$$v_t + e\left[u v_x + v v_y + w v_z\right] + fu = -h_y + \frac{d_v^2}{2} v_{zz} \qquad [2.18]$$

$$u_x + v_y + w_z = 0 \qquad [2.19]$$

Here the dimensionless parameters $f = f^* / s^*$ [2.20] (ratio of inertial and tidal frequency), $d_v = 1/H^* \sqrt{2A_v^*/s^*}$ [2.21] (square of the Stokes number) and the Froude number $e = h_0^*/H^* = U^*/\sqrt{g^* H^*}$ [2.22] are used.

2.3.2 SCALED BOUNDARY CONDITIONS

The boundary conditions at the coast transform to the following form.

$$\int_0^{1+eh} v\,dz = 0 \qquad \text{at} \qquad y = 0, B \qquad [2.23]$$

$$\int_0^{1+eh} u\,dz = 0 \qquad \text{at} \qquad x = 0 \qquad [2.24]$$

Here the non-dimensional width $B = K^* B^*$ is used. The dimensionless boundary conditions at the surface is given by

$$\begin{cases} u_z, v_z = 0 \\ w = h_t + e\left[uh_x + vh_y\right] \end{cases} \qquad \text{at} \qquad z = 1 + eh \qquad [2.25]$$

The boundary conditions at the bottom read

$$\begin{cases} s^{-1} u_z = u \\ s^{-1} v_z = v \\ w = 0 \end{cases} \qquad \text{at} \qquad z = 0 \quad , \qquad [2.26]$$

where $s^{-1} = A_v^* / \left(H^* s^*\right)$ [2.27].

2.4 LEADING-ORDER SYSTEM OF EQUATIONS

Because usually the Froude number ε<<1, the system of equations can be developed as a power series in ε. For this study the lowest order contribution in the Froude number (i.e. at $O(\varepsilon^0)$) is considered, which means that all non-linear terms are dropped from the equations and the upper vertical domain boundaries are greatly simplified. First the governing equations and then the boundary conditions will be handled.

2.4.1 LINEAR SYSTEM OF EQUATIONS

Substituting ε=0 in the governing equations it follows that no advective contribution is found and the governing equations reduce to the following linear system of equations:

$$u_t - fv = -h_x + \frac{d_v^2}{2} u_{zz}, \qquad [2.28]$$

$$v_t + fu = -h_y + \frac{d_v^2}{2} v_{zz}, \qquad [2.29]$$

$$u_x + v_y + w_z = 0. \qquad [2.30]$$

The boundary conditions at the side walls reduce to

$$\int_0^1 v dz = 0 \qquad \text{at} \qquad y = 0, B\,, \tag{2.31}$$

$$\int_0^1 u dz = 0 \qquad \text{at} \qquad x = 0 \quad . \tag{2.32}$$

At the free water surface the kinematic boundary condition is adjusted because the non-linear contribution reduces to zero, while the dynamic boundary condition stays the same. The location of the boundary reduces to z=1.

$$\begin{cases} u_z, v_z = 0 \\ w = h_t \end{cases} \qquad \text{at} \qquad z = 1 \tag{2.33}$$

The dynamic boundary condition at the flat bed, as well as the kinematic boundary condition does not change due to taking ε=0.

$$\begin{cases} s^{-1} u_z = u \\ s^{-1} v_z = v \\ w = 0 \end{cases} \qquad \text{at} \qquad z = 0 \tag{2.34}$$

3 FINDING WAVE MODES IN AN INFINITE CHANNEL

In this chapter wave solutions will be sought for an infinitely long channel. First the velocity will be transformed to rotating velocity components to aid in solving the depth-dependency of the equations. After that, relations between the longitudinal wave number and the displacement are derived. These relations are used to find a single condition which leads to two possible types of wave solutions, Kelvin waves and Poincaré modes. For these wave modes the displacement equations are found which are then used to translate the rotating velocity components back to the normal velocity components.

3.1 THE SOLUTION IN ROTATING VELOCITY COMPONENTS

In this paragraph the depth-dependency is found by solving equations for *rotating* velocity components. First the original equations are split to facilitate the solution method, after that the actual transformation is applied. The depth-independent part of the rotating components is solved first after which the depth-dependent part is also solved. The expressions for the rotating components still implicitly contain a dependency on x and y which will be handled in paragraph 3.3.

3.1.1 SPLITTING THE GOVERNING EQUATIONS AND BOUNDARY CONDITIONS

The original equations of motion (see [2.28]-[2.29]) are split by defining the velocities as $u=u_0+u_1$ and $v=v_0+v_1$ respectively. The velocities with index 0 signify the part of the velocity that is assumed not to vary in the vertical direction, leading to the following equations (after Danielson & Kowalik, 2005):

$$u_{0;t} - fv_0 = -h_x\,, \qquad [3.1]$$

$$v_{0;t} + fu_0 = -h_y\,. \qquad [3.2]$$

The depth-dependent equations with index 1 read (after Danielson & Kowalik, 2005):

$$u_{1;t} - fv_1 = \frac{d_v^2}{2}u_{1;zz}\,, \qquad [3.3]$$

$$v_{1;t} + fu_1 = \frac{d_v^2}{2}v_{1;zz}\,. \qquad [3.4]$$

To solve the equations for the rotating velocity components (which will be shown in the next paragraph) the dynamic boundary conditions for the horizontal velocities at the bottom and surface also have to be split. The slip condition becomes as follows (with $s^{-1}=0$ for no slip and $s>0$ for partial slip).

$$\begin{cases} u_1 = s^{-1}\left(u_0+u_1\right)_z - u_0 \\ v_1 = s^{-1}\left(v_0+v_1\right)_z - v_0 \end{cases} \quad \text{at} \quad z=0 \qquad [3.5]$$

The surface conditions become

$$\left(u_0+u_1\right)_z = 0 \text{ and } \left(v_0+v_1\right)_z = 0 \quad \text{at} \quad z=1 \qquad [3.6]$$

3.1.2 TRANSFORMATION TO ROTATING VELOCITY COMPONENTS

The following rotating components are introduced which (when summed) represent the current ellipses formed by the orthogonal velocities in a more convenient way (Mofjeld, 1980). Here q is the clockwise component and r is the counter clockwise component, which correspond with the distinct counter rotating layers in the bottom layer (Mofjeld, 1980). Note that $q=q_0+q_1$ [3.7] and $r=r_0+r_1$ [3.8] and that the expressions below hold for index 0 and index 1 separately.

$$q = u + iv, r = u - iv \qquad [3.9]$$

From the above it follows that

$$u = \frac{q+r}{2}, v = \frac{q-r}{2i} \qquad [3.10]$$

To represent the periodicity of the tidal flow the time-dependency of q, r and η is given by exp(-it). The second equation of motion ([3.2] and [3.4]) multiplied with the imaginary unit i is added to the first equation of motion ([3.1] and [3.3]) to yield the following:

$$q_0 = \frac{-i}{1-f}\left(h_x + ih_y\right), \qquad [3.11]$$

$$q_1 = \frac{id_v^2}{2(1-f)} q_{1;zz}. \qquad [3.12]$$

Hereby the splitting in depth-dependent and depth-independent parts will facilitate solving the equations later (see 3.1.3). When instead of an addition a subtraction is carried out the following is found:

$$r_0 = \frac{-i}{1+f}\left(h_x - ih_y\right), \qquad [3.13]$$

$$r_1 = \frac{id_v^2}{2(1+f)} r_{1;zz}. \qquad [3.14]$$

The boundary condition at the bottom translates as follows (using the same methodology as for the governing equations). It should be noted that the derivatives of q_0 and r_0 to z are both zero, which follows from the equation for q_0 and r_0 above. This condition and the condition at the surface are applied in 3.1.3.

$$\begin{aligned} q_1 &= s^{-1} q_{1;z} - q_0 \\ r_1 &= s^{-1} r_{1;z} - r_0 \end{aligned} \quad \text{at} \quad z = 0 \qquad [3.15]$$

The surface condition becomes as follows.

$$q_{1;z} = 0 \text{ and } r_{1;z} = 0 \quad \text{at} \quad z = 1 \qquad [3.16]$$

The translation of the *depth-integrated* continuity equation [2.30] to rotating velocity components yields the following. For this no difference is made between the depth-dependent and the depth-independent parts. This is because the terms that do depend on depth are integrated over depth. This condition is used in subsection 3.2.1.

$$-ih + \frac{1}{2}\int_0^1 \left(q_x - iq_y\right) + \left(r_x + ir_y\right) dz = 0 \qquad [3.17]$$

The translation of boundary conditions at the coasts [2.31] into rotating components yields the following. Also this equation does not need to be split in depth-dependent and depth-independent parts. This boundary condition is used in subsection 3.2.2.

$$\frac{1}{2i}\int_0^1 (q-r) dz = 0 \quad \text{at} \quad y = 0, B \qquad [3.18]$$

3.1.3 SOLVING THE ROTATING VELOCITY COMPONENTS

The expressions for the depth-independent rotating components [3.11] and [3.13] are solved, but the solutions for the depth-dependent components [3.12] and [3.14] are still needed. When these are found the total solution for the rotating velocity components can be derived (by adding the different parts). In the following paragraphs those expressions will be used to find the equations for η, u, v and w. To find the solutions for q_1 and r_1 first the general solution for a second-order linear ordinary differential equation is applied to the equations [3.12] and [3.14]:

$$q_1 = c_1 \exp(a_q z) + c_2 \exp(-a_q z), \qquad [3.19]$$

$$r_1 = c_3 \exp(a_r z) + c_4 \exp(-a_r z), \qquad [3.20]$$

with parameters α_q and α_r defined as

$$a_q = \frac{1-i}{d_v}(1-f)^{1/2}, \qquad [3.21]$$

$$a_r = \frac{1-i}{d_v}(1+f)^{1/2}. \qquad [3.22]$$

Applying the surface boundary condition at z=1 yields

$$(q_1)_z\big|_{z=1} = a_q c_1 \exp a_q - a_q c_2 \exp(-a_q) = 0 \rightarrow c_2 = c_1 \exp 2a_q, \qquad [3.23]$$

$$(r_1)_z\big|_{z=1} = a_r c_3 \exp a_r - a_r c_4 \exp(-a_r) = 0 \rightarrow c_4 = c_3 \exp 2a_r. \qquad [3.24]$$

At the bottom the slip condition is applied. This yields

$$q_1(0) = c_1 + c_2 = s^{-1} a_q (c_1 - c_2) - q_0 \rightarrow c_1(1 - s^{-1}a_q) + c_2(1 + s^{-1}a_q) = -q_0, \qquad [3.25]$$

$$r_1(0) = c_3 + c_4 = s^{-1} a_r (c_3 - c_4) - r_0 \rightarrow c_3(1 - s^{-1}a_r) + c_4(1 + s^{-1}a_r) = -r_0. \qquad [3.26]$$

Applying the condition for c_2 and c_4 found above gives the following result.

$$c_1 = \frac{-q_0}{1 + \exp 2a_q + s^{-1}a_q[\exp 2a_q - 1]} \rightarrow \begin{cases} c_1 = \dfrac{-q_0 \exp(-a_q)}{2[\cosh a_q + s^{-1}a_q \sinh a_q]} \\ c_2 = \dfrac{-q_0 \exp a_q}{2[\cosh a_q + s^{-1}a_q \sinh a_q]} \end{cases} \qquad [3.27]$$

$$c_3 = \frac{-r_0}{1 + \exp 2a_r + s^{-1}a_r[\exp 2a_r - 1]} \rightarrow \begin{cases} c_3 = \dfrac{-r_0 \exp(-a_r)}{2[\cosh a_r + s^{-1}a_r \sinh a_r]} \\ c_4 = \dfrac{-r_0 \exp a_r}{2[\cosh a_r + s^{-1}a_r \sinh a_r]} \end{cases} \qquad [3.28]$$

This is put back in the previously found equations for q_1 and r_1 to yield the final results.

$$q_1 = -q_0 \frac{\cosh[a_q(z-1)]}{\cosh a_q + s^{-1}a_q \sinh a_q} \qquad [3.29]$$

$$r_1 = -r_0 \frac{\cosh[a_r(z-1)]}{\cosh a_r + s^{-1}a_r \sinh a_r} \qquad [3.30]$$

Using [3.7], [3.11] and [3.29] the following is found:

$$q = \frac{-i}{1-f}\left(h_x + ih_y\right)(1-Q) \qquad [3.31] \qquad \text{with} \qquad Q(z) = \frac{\cosh\left[a_q(z-1)\right]}{\cosh a_q + s^{-1}a_q \sinh a_q} \qquad [3.32]$$

And analogous to the above for [3.8], [3.13] and [3.30] the following is found.

$$r = \frac{-i}{1+f}\left(h_x - ih_y\right)(1-R) \qquad [3.33] \qquad \text{with} \qquad R(z) = \frac{\cosh\left[a_r(z-1)\right]}{\cosh a_r + s^{-1}a_r \sinh a_r} \qquad [3.34]$$

Here the new parameters Q and R determine the vertical pattern of the rotating velocity components. The expressions for Q and R reduce to those found by Mofjeld (1980) if s^{-1}=0 (no slip), though in non-dimensional form.

3.2 DETERMINING WAVENUMBER RELATIONS

In this paragraph a dispersion relation and a new version of the coastal boundary conditions will be derived which define the relation between the longitudinal wave number and the displacement. These relations are used in the next paragraph.

3.2.1 DISPERSION RELATION

The rotating components q and r are substituted in the depth-integrated continuity equation [2.30], which, after some manipulation, yields the following result.

$$h_{xx} + h_{yy} + \frac{1-f^2}{H_e}h = 0 \qquad [3.35]$$

For clarity a new parameter H_e was introduced, which is shown below.

$$H_e = 1 - \frac{1}{2}\left[\frac{(1+f)\sinh a_q}{a_q\left[\cosh a_q + s^{-1}a_q \sinh a_q\right]} + \frac{(1-f)\sinh a_r}{a_r\left[\cosh a_r + s^{-1}a_r \sinh a_r\right]}\right] \qquad [3.36]$$

This dispersion equation is the same as the inviscid dispersion equation except that this equation is corrected with the parameter H_e which accounts for viscous effects and the effects of the partial slip condition. As can be expected the expression for H_e reduces to the expression found by Mofjeld (1980) when derived from the dimensional form of the dispersion relation and with s^{-1}=0 (no slip). Equation [3.35] allows for solutions of the following form, where $\bar{h}(y)$ is a y-dependent function and k the wave number of this wave solution.

$$h = \Re\left[\bar{h}(y)\exp\left(i(kx-t)\right)\right] \qquad [3.37]$$

This wave equation is substituted in [3.35] to obtain the dispersion relation.

$$k^2 - \frac{\bar{h}_{yy}}{\bar{h}} = \frac{1-f^2}{H_e} \qquad \text{or} \qquad \bar{h}_{yy} + \left(\frac{1-f^2}{H_e} - k^2\right)\bar{h} = 0 \qquad [3.38]$$

3.2.2 NEAR-COASTAL BOUNDARY CONDITIONS

Applying the near-coastal boundary condition ([3.18]) yields the following after some manipulation.

$$\bar{h}_y + k\frac{g}{H_e}\bar{h} = 0 \qquad \text{at} \qquad y = 0, B \qquad [3.39]$$

Here the parameters H_e and γ were substituted into the equation to yield the final result. H_e was already shown in the previous paragraph, while γ is shown below.

$$g = f - \frac{1}{2}\left[\frac{(1+f)\sinh a_q}{a_q\left[\cosh a_q + s^{-1}a_q \sinh a_q\right]} - \frac{(1-f)\sinh a_r}{a_r\left[\cosh a_r + s^{-1}a_r \sinh a_r\right]}\right] \qquad [3.40]$$

This parameter is similar to H_e but is a correction applied to f rather than to 1. As can be expected the expression for γ reduces to the expression found by Mofjeld (1980) when made dimensional again and with $s^{-1}=0$ (no slip).

3.3 *SOLVING THE WAVENUMBER RELATIONS*

The general solution to [3.38] reads

$$\bar{h} = C\sin ay + D\cos ay \qquad [3.41] \qquad \text{with} \qquad a^2 = \frac{1-f^2}{H_e} - k^2. \qquad [3.42]$$

Substituting this solution into the boundary condition ([3.39]),

$$a\left(C\cos ay - D\sin ay\right) + k\frac{g}{H_e}\left(C\sin ay + D\cos ay\right) = 0 \qquad \text{at} \qquad y = 0, B. \qquad [3.43]$$

Substituting y=0,B in [3.43] yields the following set of equations for C and D:

$$aC + k\frac{g}{H_e}D = 0, \qquad [3.44]$$

$$C\left[a\cos aB + k\frac{g}{H_e}\sin aB\right] + D\left[k\frac{g}{H_e}\cos aB - a\sin aB\right] = 0. \qquad [3.45]$$

This system of equations leads to nontrivial solutions for C and D when the determinant equals zero. Taking the determinant, substituting the relation for α [3.42] and rearranging, leads to the following condition for nontrivial solutions:

$$\left[\frac{(1-f^2)H_e}{H_e{}^2 - g^2} - k^2\right]\sin aB = 0. \qquad [3.46]$$

In the following paragraphs the two cases will be analysed for which the condition above is met.

3.3.1 SATISFYING WAVENUMBER RELATIONS WITH KELVIN WAVES

The condition [3.46] is met when k_0 (index 0 signifies the Kelvin wave) satisfies (derived from [3.46])

$$k^2 = k_0^2 = \frac{(1-f^2)H_e}{H_e{}^2 - g^2} \text{ or } k_0 = \left\{\frac{(1-f^2)H_e}{H_e{}^2 - g^2}\right\}^{1/2}. \qquad [3.47]$$

The positive root for k_0 is chosen, so that the wave travels in the positive x-direction (it therefore represents the outgoing Kelvin wave). With a negative wave number the wave would travel in the negative x-direction (and would be the incoming Kelvin wave). The above combined with the relation for α yields the following.

$$a^2 = a_0^2 = -\frac{k_0^2 g^2}{H_e^2} \text{ or } a_0 = i\frac{k_0 g}{H_e} \qquad [3.48]$$

Also here the positive root is chosen, because the negative root gives no extra information (it would be the same as choosing a negative value for k_0 above, also see Pedlosky, 1982 and De Swart, 2008).

To find the equation for the free surface displacement, the first equation for C and D [3.44] is transformed.

$$C = -\frac{k_0 g}{a_0 H_e} D \qquad [3.49]$$

Value of D is for now set to unity, as η will be re-scaled with η_0* eventually to find η*. The parameter D therefore serves no real function, as the actual amplitude will be determined by η_0*. The relation for C is substituted in the relation for $\bar{h}$ [3.41]. After substituting the relation for α [3.48] for which a Kelvin wave is found and some final rearranging, the expression for the lateral dependency of the surface displacement is found to be

$$\bar{h}(y) = \exp(-yk_0 g / H_e), \qquad [3.50]$$

which is used in equation [3.37].

To transform the rotating velocity components back into the normal velocity components the spatial derivatives of the surface displacement are needed. These are substituted into the equations for the rotating components [3.31] and [3.33]. Using the relation between the normal and rotating velocity components [3.10] the following is eventually found for the velocity components.

$$u = \Re\left\{\frac{ik_0\bar{h}\exp(i(k_0 x - t))}{2}\left[\bar{Z}\left(1-\frac{g}{H_e}\right)+\hat{Z}\left(1+\frac{g}{H_e}\right)\right]\right\} \qquad [3.51]$$

$$v = \Re\left\{\frac{k_0\bar{h}\exp(i(k_0 x - t))}{2}\left[\bar{Z}\left(1-\frac{g}{H_e}\right)-\hat{Z}\left(1+\frac{g}{H_e}\right)\right]\right\} \qquad [3.52]$$

Here $\bar{Z}(z) = -i[1-Q(z)](1-f)^{-1}$ [3.53] and $\hat{Z}(z) = -i[1-R(z)](1+f)^{-1}$ [3.54], with Q and R defined in [3.32] and [3.34] respectively. To find the vertical velocity w the spatial derivatives of the velocities u and v are needed (see the continuity equation [2.30]). The bottom and surface boundary conditions are used to find the final expression for w, which reads:

$$w = \Re\left[\frac{k_0^2\bar{h}(y)\exp(i(k_0 x - t))}{2}\left(1-\frac{g^2}{H_e^2}\right)\tilde{\bar{Z}}\right], \qquad [3.55]$$

with

$$\tilde{\bar{Z}}(z) = \frac{-i}{1-f}\left(z-\frac{1}{a_q}\frac{\sinh[a_q(z-1)]+\sinh a_q}{\cosh a_q + s^{-1}a_q \sinh a_q}\right)+\frac{-i}{1+f}\left(z-\frac{1}{a_r}\frac{\sinh[a_r(z-1)]+\sinh a_r}{\cosh a_r + s^{-1}a_r \sinh a_r}\right). \qquad [3.56]$$

3.3.2 SATISFYING WAVENUMBER RELATIONS WITH POINCARÉ MODES

The condition $\sin aB = 0$ follows from expression [3.46] and is met when

$$a = a_n = \frac{np}{B}, \qquad n = 1,2,3,.... \qquad [3.57]$$

Herein α_n=0 is not a valid solution because [3.41] then reduces to $\bar{h}(y) = D$, which means it will have no lateral variation. The lateral velocity is however non-zero; both factors combined means that such a wave cannot meet the condition of vanishing depth-integrated normal flow through the walls (Pedlosky, 1982). Combining the relation above with the previously found equation for α^2 [3.42] gives the following.

$$a_n^2 = \frac{1-f^2}{H_e} - k^2 = \frac{n^2 p^2}{B^2} \qquad [3.58]$$

As in the previous section here the positive root of α is chosen. For this problem the tidal frequency is given (M2-tide), but the wavenumber is unknown so the relation above is transformed to find the wavenumber

$$k = k_n = \pm\left\{\frac{1-f^2}{H_e} - \frac{n^2 p^2}{B^2}\right\}^{1/2}. \qquad [3.59]$$

As in the previous section here the positive root is chosen. To find the equation for the free surface displacement the relation [3.44] for α is transformed.

$$C = -\frac{k_n g}{a_n H_e} D \qquad [3.60]$$

The parameter D is called η_n (with $\eta_n = \eta_n^* / \eta_0^*$) from now on. The relation for C is substituted in the relation for $\bar{h}_n$ [3.41] (the subscript n is added for clarity). After substituting the relation [3.58] for α for which Poincaré modes are found and some final rearranging the expression for the lateral dependency of the surface displacement is found.

$$\bar{h}_n(y) = \cos(a_n y) - \frac{B k_n}{np}\frac{g}{H_e}\sin(a_n y) \qquad [3.61]$$

To transform the rotating velocity components back into the normal velocity components the spatial derivatives of the surface displacement are needed. These are substituted into the equations for the rotating components [3.31] and [3.33]. Using the relation between the normal and rotating velocity components [3.10] the following is found for the velocity components.

$$\begin{cases} u_n = \Re\left\{\dfrac{i h_n \exp(i(k_n x - t))}{2}\left[k_n \bar{h}_n * \left(\bar{Z} + \hat{Z}\right) + \hat{h}_n * \left(-\bar{Z} + \hat{Z}\right)\right]\right\} \\ v_n = \Re\left\{\dfrac{h_n \exp(i(k_n x - t))}{2}\left[k_n \bar{h}_n * \left(\bar{Z} - \hat{Z}\right) + \hat{h}_n * \left(-\bar{Z} - \hat{Z}\right)\right]\right\} \end{cases} \qquad [3.62]$$

where $\hat{h}_n(y) = \left[\frac{np}{B}\sin(a_n y) + k_n \frac{g}{H_e}\cos(a_n y)\right]$ [3.63]

To find w the spatial derivatives of the velocities u and v are needed (see the continuity equation [2.30]. The bottom and surface boundary conditions are used to find the final expression for w, which reads:

$$w_n = \Re\left[\frac{h_n \exp(i(k_n x - t))}{2}\left(\frac{1-f^2}{H_e}\right)\bar{h}_n \tilde{Z}\right], \qquad [3.64]$$

with $\tilde{Z}$ as defined before in equation [3.56].

4 WAVE MODES IN SEMI-ENCLOSED BASINS

In this chapter a solution for tidal flow in a semi-enclosed basin is found. The Kelvin wave described before travels along the positive x-direction and is therefore the outgoing Kelvin wave. In the first paragraph the expressions for the incoming Kelvin wave are derived. After that, depth-averaged versions of the expressions for the outgoing Kelvin wave are presented (the incoming versions can be derived analogously). In the final paragraph these depth- averaged expressions will be used to find the amplitudes of the different wave modes by applying the lateral boundary condition [2.32] with a collocation method.

4.1 KELVIN WAVES

The expressions that were derived before ([3.50], [3.51], [3.52] and [3.55]) apply to the outgoing Kelvin wave in an infinite channel but could have been derived for an incoming Kelvin wave as well. Because this incoming wave is needed as well the necessary adjustments to the original expressions are described below.

The incoming Kelvin wave enters the system from the right and travels towards the lateral boundary at x=0 (see Figure 2). The direction of the horizontal velocities of the incoming wave must be opposite to that of the outgoing wave. The expressions for the outgoing wave can be easily adjusted by taking the negatives of these velocities.

The incoming wave has its highest amplitude there were it enters the system, because due to the viscosity terms in the governing equations the wave experiences energy dissipation over distance, see paragraph 5.1.2. To ensure that the longitudinal dependency is correct the negative wave number k_0 is used for the incoming wave (ik_0x **à** $-ik_0x$).

The amplitude of the incoming Kelvin wave's elevation and velocities must decrease with *decreasing* y (i.e. when moving away from the *upper* coast, see Figure 2). The expressions for the outgoing Kelvin wave of course let the amplitude decrease with *increasing* y (i.e. when moving away from the *lower* coast); therefore a negative lateral coordinate is used for the lateral dependency. Furthermore, to ensure that both the incoming and outgoing Kelvin waves have the same value for $\bar{h}$ at the upper and lower coast respectively (i.e. to ensure symmetry), the argument of expression [3.50] for $\bar{h}$ of the incoming wave is adjusted (y **à** B-y).

These transformations are applied to the expressions found in 3.3.1 ([3.50], [3.51], [3.52] and [3.55]), resulting in the following equations for the incoming Kelvin wave:

$$h_{in} = \Re\left[\bar{h}(B-y)\exp\left(-i\left(k_0 x+t\right)\right)\right], \qquad [4.1]$$

$$u_{in} = \Re\left\{\frac{-ik_0\bar{h}(B-y)\exp\left(-i\left(k_0 x+t\right)\right)}{2}\left[\bar{Z}\left(1-\frac{g}{H_e}\right)+\hat{Z}\left(1+\frac{g}{H_e}\right)\right]\right\}, \qquad [4.2]$$

$$v_{in} = \Re\left\{\frac{-k_0\bar{h}(B-y)\exp\left(-i\left(k_0 x+t\right)\right)}{2}\left[\bar{Z}\left(1-\frac{g}{H_e}\right)-\hat{Z}\left(1+\frac{g}{H_e}\right)\right]\right\}, \qquad [4.3]$$

$$w_{in} = \Re\left[\frac{k_0^2\bar{h}(B-y)\exp\left(-i\left(k_0 x+t\right)\right)}{2}\left(1-\frac{g^2}{H_e^2}\right)\tilde{Z}\right]. \qquad [4.4]$$

For the outgoing Kelvin wave the original expressions are of course still correct and will be used to describe tidal flow in a semi-enclosed basin. It should be noted that due to dissipation the outgoing wave will have a lower amplitude than the incoming wave. To make sure this can be modelled

accordingly the incoming expressions are multiplied by a reflection coefficient R; the value of this coefficient will be calculated with a collocation method (see paragraph 4.3).

4.2 THE DEPTH-AVERAGED MODEL

In this paragraph depth-averaged equations for the horizontal velocities of the Kelvin waves and Poincaré modes will be derived. To ensure there is no normal depth-averaged flow through the lateral boundary, the numerical approach presented in paragraph 4.3 will use the expression for the longitudinal velocity.

4.2.1 DEPTH-AVERAGED VELOCITIES OF A KELVIN WAVE

The horizontal along channel velocity u of a Kelvin wave will be integrated over the entire water column. For this only the part between square brackets in the following expression will be integrated as only the $\overline{Z}$ and $\hat{Z}$ parameters are dependent on the vertical position.

$$\langle u \rangle \equiv \int_0^1 u\,dz = \Re\left\{\int_0^1 \frac{ik_0\overline{h}\exp(i(k_0x-t))}{2}\left[\overline{Z}\left(1-\frac{g}{H_e}\right)+\hat{Z}\left(1+\frac{g}{H_e}\right)\right]dz\right\} \quad [4.5]$$

After integration, substitution of the parameters k, γ and H_e and some rearranging the following result is obtained.

$$\langle u \rangle = \Re\frac{\overline{h}\exp(i(k_0x-t))}{k_0} \quad [4.6]$$

The depth-averaged horizontal lateral velocity v of a Kelvin wave is derived in similar manner.

$$\int_0^1 v\,dz = \langle v \rangle = \Re\left\{\int_0^1 \frac{k_0\overline{h}\exp(i(k_0x-t))}{2}\left[\overline{Z}\left(1-\frac{g}{H_e}\right)-\hat{Z}\left(1+\frac{g}{H_e}\right)\right]dz\right\} \quad [4.7]$$

After integration and some rearranging the following result is obtained.

$$\langle v \rangle = \Re\left[\frac{ik_0\overline{h}\exp(i(k_0x-t))}{2} * \frac{2}{1-f^2}\left(-g-\frac{g}{H_e} * -H_e\right)\right] = 0 \quad [4.8]$$

This shows that boundary condition of zero normal depth-integrated flow at the channel boundaries is indeed satisfied by a Kelvin wave. This condition even leads to the property that the depth-averaged lateral velocity is zero over the *entire* width of the basin.

4.2.2 DEPTH-AVERAGED VELOCITIES OF POINCARÉ MODES

The horizontal along channel velocity u of a Poincaré mode is integrated analogous to that of the Kelvin wave.

$$\int_0^1 u_n\,dz = \langle u \rangle = \Re\left\{\int_0^1 \frac{ih_n\exp(i(k_nx-t))}{2}\left\{k_n\overline{h}_n * \left[\overline{Z}+\hat{Z}\right]+\hat{h}_n * \left[-\overline{Z}+\hat{Z}\right]\right\}dz\right\} \quad [4.9]$$

After integration and some rearranging the following result is obtained.

$$\langle u \rangle = \Re\left\{\frac{k_nh_n\exp(i(k_nx-t))}{1-f^2}\left(H_e\overline{h}_n - g\hat{h}_n\right)\right\} \quad [4.10]$$

Also the horizontal lateral velocity v of a Poincaré mode is integrated over the entire water column.

$$\int_0^1 v_n dz = \langle v \rangle = \Re \int_0^1 \left\{ \frac{h_n \exp(i(k_n x - t))}{2} \left[k_n \bar{h}_n * \left(\bar{Z} - \hat{Z} \right) + \hat{h}_n * \left(-\bar{Z} - \hat{Z} \right) \right] \right\} \quad [4.11]$$

After integration and some rearranging the following result is obtained.

$$\langle v \rangle = \Re \left[\frac{i h_n \exp\left(i \left(k_n x - t \right) \right)}{1 - f^2} * \left(\frac{k_n^{\,2}}{a_n} \frac{g^2}{H_e} + a_n H_e \right) \sin\left(a_n y \right) \right] \quad [4.12]$$

The above shows that the depth-integrated lateral velocity of a Poincaré mode is not zero for all x, y and t (as opposed to a Kelvin wave). However, substituting y=0,B shows that the depth-integrated normal flow is indeed zero at the boundaries for a Poincaré mode.

4.3 SUPERIMPOSING THE WAVE SOLUTIONS

Here a solution to the tidal flow problem in a semi-enclosed basin is presented as a superposition of an incoming Kelvin wave, an outgoing Kelvin wave (with a reflection coefficient R) and an infinite number of Poincaré modes (where the amplitude depends on n). It should however be noted that for calculations not the *infinite* set of Poincaré modes is included (which would of course be impossible), but a truncated set of N Poincaré modes, which means that a total of N + 2 modes will be summed. For increasing N the solution comes closer to the exact solution, but it is expected that a set in the order of tens of Poincaré modes will lead to good results. The expressions for total displacement and velocities are as follows.

$$h_{total}(x, y, z, t) = h_{in} + h_{out} + \sum_{n=1}^{N} h_n \quad [4.13]$$

$$u_{total}(x, y, z, t) = u_{in} + u_{out} + \sum_{n=1}^{N} u_n \quad [4.14]$$

$$v_{total}(x, y, z, t) = v_{in} + v_{out} + \sum_{n=1}^{N} v_n \quad [4.15]$$

$$w_{total}(x, y, z, t) = w_{in} + w_{out} + \sum_{n=1}^{N} w_n \quad [4.16]$$

Of the N+2 modes the amplitude of the incoming Kelvin wave is a given. The relative amplitudes of the remaining N+1 modes (R and $\eta_{0;n}/\eta_0$) will be sought with the method described below. For this method conditions will be derived which the depth-integrated normal velocity must meet at the lateral boundary (at x=0). This leads to the following expression for u_{total} as function of y and t.

$$\langle u_{total}(y,t) \rangle = \Re \left\{ \frac{1}{k_0} \left[-\bar{h}(B - y) \exp(-it) + R * \bar{h} \exp(it) \right] + \sum_{n=1}^{N} \frac{k_n h_n \exp(it)}{1 - f^2} \left(H_e \bar{h}_n - g \hat{h}_n \right) \right\} \quad [4.17]$$

The collocation method finds the appropriate amplitudes of the separate modes by minimising the depth-integrated normal velocity for a fixed set of points at the lateral boundary. The N+1 collocation points have the following (x,y)-coordinates.

$$(0, y_m) \qquad \text{with} \qquad y_m = \frac{m-1}{N} B \qquad \text{for} \qquad m = 1,2,\ldots, N+1 \quad [4.18]$$

The depth-integrated velocity in the x-direction (alongshore) must be zero at these N+1 collocation points. The aforementioned translates to the following desired state (which should be met for all t).

$$\langle u_{total} \rangle = 0 \quad \text{at} \quad (x, y) = (0, y_m) \quad \text{for} \quad m = 1,2,\ldots, N+1 \quad [4.19]$$

Because this condition must be met all moments during the tidal cycle an expression for $<u_{total}>$ that only depends on the lateral coordinate y is needed. Using equations [4.17] and [4.19] the following is derived:

$$\frac{1}{k_0}\left[-\bar{h}(B-y)+R*\bar{h}\right]+\sum_{n=1}^{N}\frac{k_n h_n}{1-f^2}\left\{H_e\bar{h}_n-g\hat{h}_n\right\}=0. \qquad [4.20]$$

This must hold at $y=y_m$ for $m=1,2,...,N+1$. The condition is written in the following form for simplicity.

$$A_{K;in}(y_m)+RA_{K;out}(y_m)+\sum_{n=1}^{N}h_n A_P(y_m,n)=0 \quad \text{at} \quad y=y_m \quad \text{for} \quad m=1,2,...,N+1 \qquad [4.21]$$

Hereby $A_{K;in}$, $A_{K;out}$ and A_P are defined as (with expressions for $\bar{h}$, $\bar{h}_n$ and $\hat{h}_n$ substituted):

$$\left.\begin{aligned}
A_{K;in} &= -\frac{1}{k_0}\exp\left(-(B-y)k_0 g/H_e\right)\\
A_{K;out} &= \frac{1}{k_0}\exp\left(-y\,k_0 g/H_e\right)\\
A_P &= \frac{k_n}{1-f^2}\left\{H_e\left[\cos(a_n y)-\frac{k_n}{a_n}\frac{g}{H_e}\sin(a_n y)\right]-\left[\frac{a_n}{k_n}\sin(a_n y)+\frac{g}{H_e}\cos(a_n y)\right]*g\right\}
\end{aligned}\right\}. \qquad [4.22]$$

In matrix-form the previous condition is as follows:

$$\begin{bmatrix}
A_{K;out}(y_1) & A_P(y_1,1) & A_P(y_1,2) & \text{M} & A_P(y_1,N)\\
A_{K;out}(y_2) & A_P(y_2,1) & A_P(y_2,2) & \text{M} & A_P(y_2,N)\\
\mathbf{K} & \mathbf{K} & \mathbf{K} & \mathbf{O} & \mathbf{K}\\
A_{K;out}(y_N) & A_P(y_N,1) & A_P(y_N,2) & \text{M} & A_P(y_N,N)\\
A_{K;out}(y_{N+1}) & A_P(y_{N+1},1) & A_P(y_{N+1},2) & \text{M} & A_P(y_{N+1},N)
\end{bmatrix}*\begin{bmatrix} R\\ h_1\\ h_2\\ \text{M}\\ h_N\end{bmatrix}=\begin{bmatrix}
-A_{K;in}(y_1)\\ -A_{K;in}(y_2)\\ \mathbf{L}\\ -A_{K;in}(y_N)\\ -A_{K;in}(y_{N+1})
\end{bmatrix}. \qquad [4.23]$$

The amplitude vector is then determined using standard techniques in The Mathworks™ MATLAB®.

5 FLOW PROPERTIES OF THE SOLUTION

Properties of the wave solutions have been examined for the Northern part of the North Sea (see Figure 3), as that basin approximately is a semi-enclosed basin and has dimensions that match the assumptions and conditions used to derive the governing equations and boundary conditions. The basin is approximately 500 km wide and has an average depth of 65 m (taken from Davies & Jones (1995), also see figure below). The model derived uses a constant Coriolis frequency, therefore an average latitude of 55° is used.

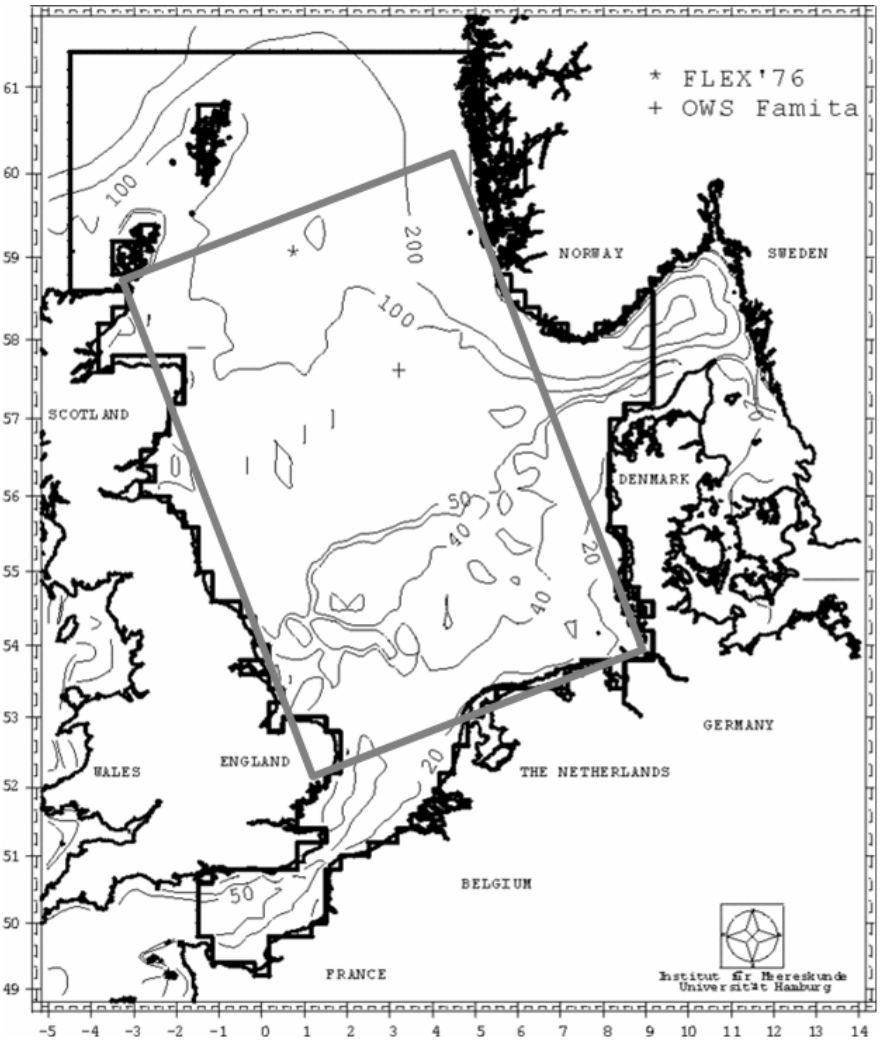

Figure 4: bathymetry of the North Sea in meters (source: http://www.ifm.zmaw.de/)

The Coriolis frequency then follows from $f^* = 2\Omega^* \sin q^*$ [5.1], with Ω^* the angular frequency of the Earth's rotation and θ* latitude. The vertical viscosity parameter A_v* is calculated with $A_v^* = 0.0025 U^* H^*$ [5.2]; this relation taken from Bowden (1967) models the observed maximum eddy viscosity in tidal currents in homogeneous water. The author actually uses the depth-mean amplitude of the current instead of the typical Kelvin wave velocity U*, with the latter probably smaller than the former. It is assumed this is compensated because the *maximum* eddy viscosity parameter instead of an average is taken. For this case the principal semidiurnal tidal constituent as caused by the gravitational pull of the Moon (M2 tide) is used as the tidal forcing. The period T* of this constituent is 12 hours and 25 minutes and the tidal frequency is defined as $s^* = 2p/T^*$. The

gravity constant g* is 9.81m/s^2 for this part of the Earth. The amplitude of tidal elevation η_0* is a suitable value for that part of the North Sea taken from Sinha & Pingree (1997). The value for the slip parameter s* is taken from Davies & Jones (1995). In the table below the dimensional values are given for the mentioned parameters.

	Value	
H*	65	m
B*	500	km
θ*	55	°
f*	1.19E-04	s^{-1}
A_v*	0.0947	m^2/s
η_0*	1.5	m
σ*	1.41E-04	s^{-1}
g*	9.81	m/s^2
s*	0.005	m/s

Table 1: model parameters of the Northern part of the North Sea

The model is implemented in The Mathworks™ MATLAB® and runs with a truncated set of Poincaré modes (N=20). Properties of the wave numbers, individual wave modes and the total solution will be presented in the following paragraphs.

5.1 PROPERTIES OF THE INDIVIDUAL MODES

In this paragraph properties of the individual modes are studied. First the wave numbers are handled, then certain aspects of Kelvin and Poincaré modes are examined and finally a translation is made between the used 3D friction model (with A_v* and s*) and a depth-averaged model (2DH, using a friction parameter r_{fr}*).

5.1.1 WAVE NUMBERS OF KELVIN AND POINCARÉ MODES

In the following wave number plots the results for different values of the viscosity A_v* (with different markers) are plotted for the different wave modes (see Figure 5 and Figure 6). The resulting wave numbers have been made dimensional again; see Appendix B for how various parameters are made dimensional again. A_v* varies between 0.013 and 10 times the reference value mentioned above, the lower limit is chosen because MATLAB could not compute the results for lower values.

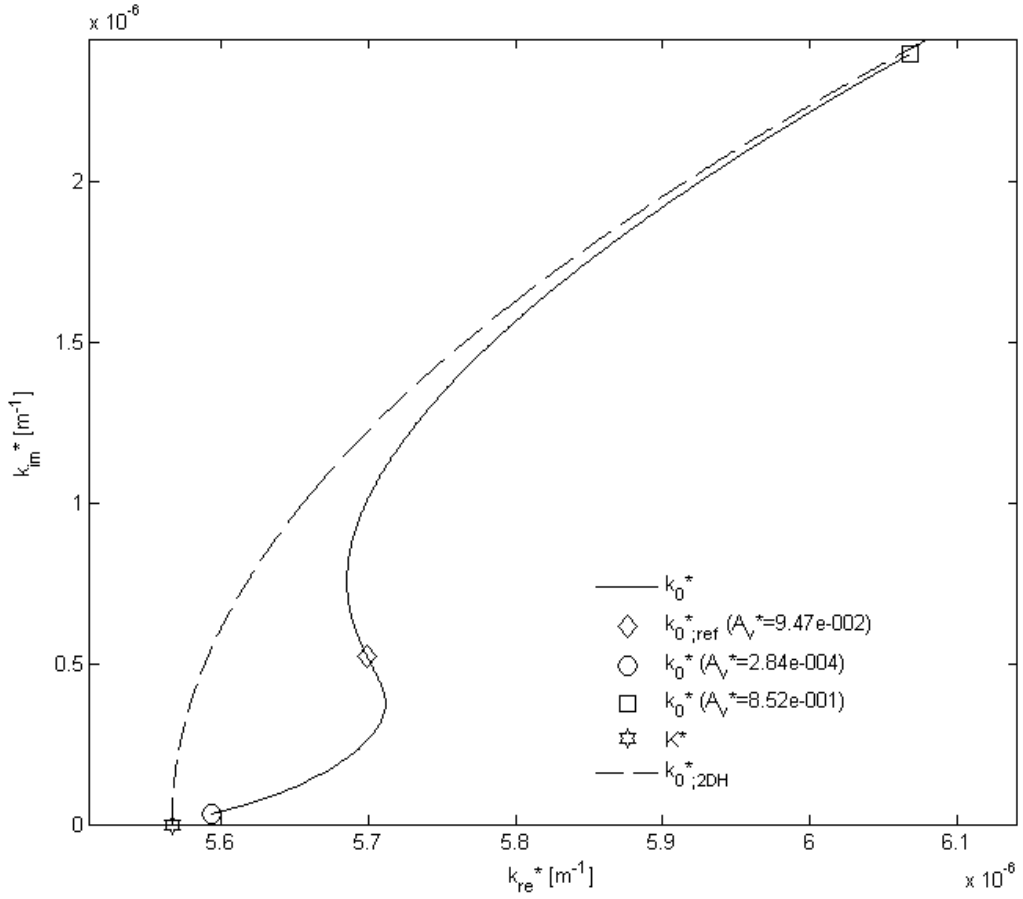

Figure 5: wave numbers k_0* in the complex wave number plane for different values of A_v* [m^2/s]

In the figure above the wave numbers k_0* of only the Kelvin wave are plotted, alongside the inviscid wave number K* and (as a reference) the wave number $k_{0;2DH}$* of a depth-averaged Kelvin wave (for varying friction parameter r_{fr}*). It should be noted that for all depth-averaged calculations the model presented by Rienecker & Teubner (1980) is used (see Appendix C).

For the Kelvin wave the real and imaginary part of the wave number increases with increasing viscosity and friction parameter (the former is also observed by Mofjeld, 1980). This signifies that the Kelvin wave shows increased dissipation while also its propagating character becomes stronger. This can be explained by looking at the expression for the wave number [3.47], which uses the parameters H_e [3.36] and γ [3.40]. These parameters have a depth-integrated contribution of the clockwise and counter clockwise components Q [3.32] and R [3.34]. This complex interaction (with hyperbolic cosines and sines) leads to the development of the wave number and also causes the 'bump' in the graph above for the 3D model. In paragraph 5.1.2 it will be investigated what the net effect (more dissipation or more propagation) of increasing A_v* is on the 3D Kelvin wave. With decreasing A_v* and r_{fr}*, the imaginary part of the wave number of the Kelvin wave approaches zero and the real part approaches the inviscid wave number K*. This is to be expected, because when these values decrease the dissipation mechanism is 'shut down' and the properties should resemble that of an inviscid wave.

In the following figure the wave numbers for all Kelvin and Poincaré modes are plotted in the complex plane for varying viscosity (the rate in the legend is multiplied with A_v* of the reference case to get the used value).

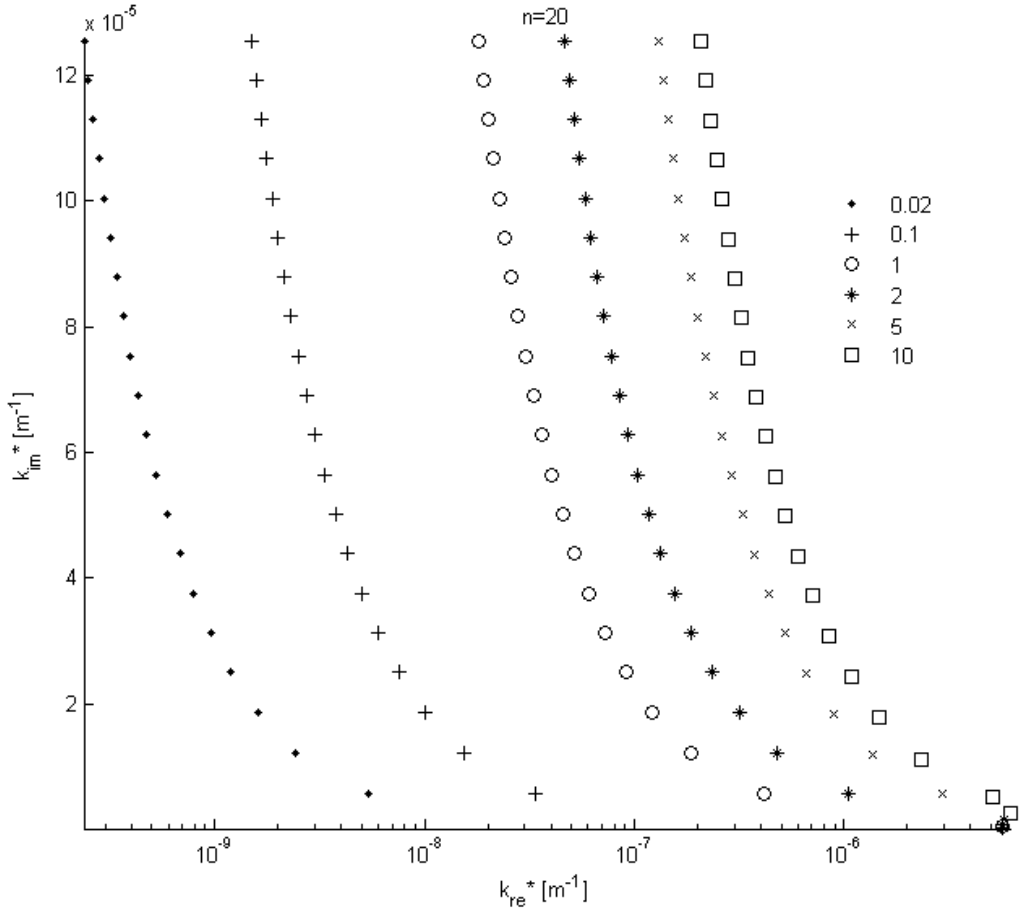

Figure 6: wave numbers in the complex wave number plane for different values of A_v* [m^2/s]

In the figure above, per value of A_v* (the value in the legend multiplied with A_v* of the reference case), the mode with n=0 (the Kelvin wave) has the highest real part of the wave number and the lowest imaginary part (they all plot in the lower right corner of the plot). With increasing n (increasingly higher Poincaré modes) the imaginary part increases, while the real part decreases. This signifies that the dissipative character of higher modes is stronger than that of lower modes. The Poincaré modes have a wave number that is partly real and partly imaginary. If the wave number would be purely imaginary the Poincaré modes would only exist directly at the coast, they would be *bound*. With a purely real wave number they would freely propagate throughout the channel, they would be *free*. In this case they are neither completely free nor bound, but because the imaginary part is generally much bigger than the real part their influence in the basin is limited to a small area and they can be practically called bound.

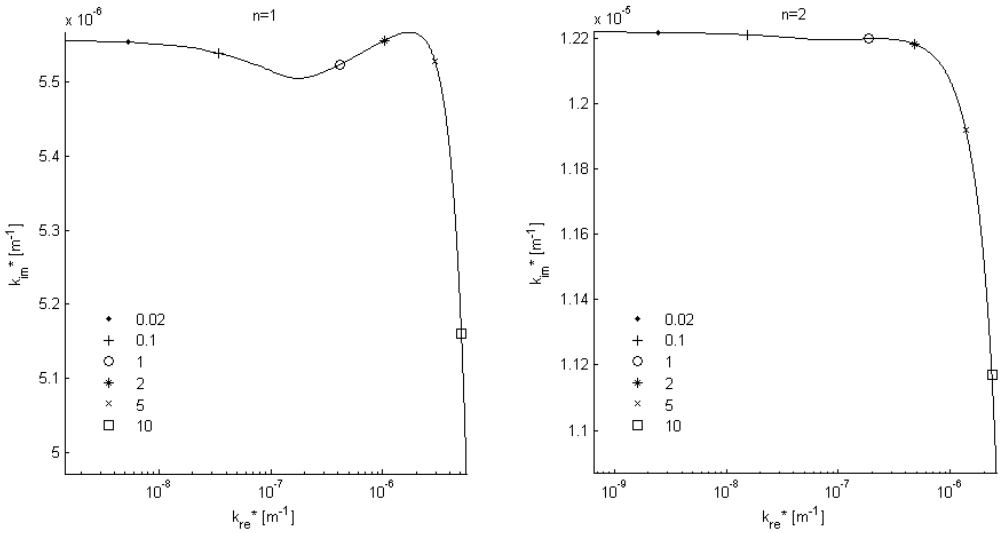

Figure 7: Poincaré wave numbers (n=1,2) in the complex wave number plane for varying $A_v^*/A_{v;ref}^*$

The following can be more clearly observed in the figures above for two separate Poincaré modes than in the plot with all wave numbers. With increasing A_v^* the real part becomes larger for all Poincaré modes while the imaginary part shows a slight decrease, but only on the *left* side of the plot (for the *smaller* viscosity). On the *right* side of the plot there is a (slight increase) of the imaginary part with increasing A* before dropping off when the viscosity gets very high. This is due to the interaction between the clockwise and counter clockwise components Q and R, which in depth-integrated form influence the Poincaré wave number through H_e (see expressions [3.32], [3.34] and [3.36].).

5.1.2 PROPERTIES OF THE KELVIN WAVE

The wave length of the Kelvin wave λ is determined by $l = 2p / k_{0;re}$ [5.3] with k_0 the wave number of the Kelvin wave. The wave length indicates the progressive character of the Kelvin wave. The ratio D of the Kelvin wave amplitudes at two locations separated by one wavelength in the longitudinal direction shows the relative effect of the dissipation caused by inclusion of viscosity terms. This is given by $D = \exp\left(-2pk_{0;im} / k_{0;re}\right)$ [5.4]. In the table below rate=$A_v^*/A_v^*_{ref}$ where the values with subscript 'ref' are from the reference case. Furthermore the resulting values for the wave number k_0, wave length λ and decay ratio D are given.

rate	0.01	0.1	1	2	5	10
k_0 (m^{-1})	5.61e-006+ 5.52e-008i	5.68e-006+ 1.76e-007i	5.70e-006+ 5.21e-007i	5.69e-006+ 8.00e-007i	5.80e-006+ 1.55e-006i	6.15e-006+ 2.59e-006i
λ (km)	1119	1107	1102	1105	1084	1022
D	0.94	0.82	0.56	0.41	0.19	0.07

Table 2: Kelvin wave properties

The table shows that for increasing viscosity (the increasing parameters increase linearly with increasing A_v^*), the wave length first increases and then decreases, showing that the propagative character in itself first becomes stronger and then weaker which is due to the development of the Kelvin wave number (see 5.1.1). However, as the decay factor D keeps getting smaller regardless of whether propagation increases or decreases, the increase of dissipation is stronger.

5.1.3 PROPERTIES OF THE POINCARÉ MODES

In the inviscid case for $B<B_{crit}$ with $B_{crit} = p\sqrt{\left(1-f^2\right)^{-1}}$ all Poincaré modes have a purely imaginary wave number (and are therefore bound, also see 5.1.1). However due to the addition of viscous effects the free modes gain a slightly dissipative character (the wave number is no longer purely real), while the bound modes gain a slightly propagating character (the wave number is no longer purely imaginary), like mentioned in Roos & Schuttelaars (2009) for horizontal viscous effects. The authors state that for small values of the horizontal viscosity and friction these modifications are small so that the condition $B<B_{crit}$ used in the inviscid case that says whether Poincaré modes are free or bound can still be used. It is assumed that this also applies for the current case (vertical viscosity). In the reference case B_{crit}* is 1071 km and B* is 500 km, so all Poincaré modes are bound.

In the table below the Poincaré wave numbers as well as the e-folding decay lengths are given (determined by $L_n = k_{n;im}^{-1}$). In this table it can be seen that increasingly higher Poincaré modes have less influence in the channel as they decay over a smaller distance.

n	k_n (m^{-1})	L_n (km)
1	4.05e-007+5.52e-006i	181.000
2	1.83e-007+1.22e-005i	82.000
3	1.20e-007+1.86e-005i	53.700
4	8.97e-008+2.50e-005i	40.100
5	7.15e-008+3.13e-005i	32.000
6	5.95e-008+3.76e-005i	26.600
7	5.10e-008+4.39e-005i	22.800
8	4.46e-008+5.02e-005i	19.900
9	3.96e-008+5.65e-005i	17.700
10	3.56e-008+6.28e-005i	15.900
11	3.24e-008+6.90e-005i	14.500
12	2.97e-008+7.53e-005i	13.300
13	2.74e-008+8.16e-005i	12.300
14	2.54e-008+8.79e-005i	11.400
15	2.37e-008+9.42e-005i	10.600
16	2.23e-008+1.00e-004i	9.950
17	2.10e-008+1.07e-004i	9.370
18	1.98e-008+1.13e-004i	8.850
19	1.87e-008+1.19e-004i	8.380
20	1.78e-008+1.26e-004i	7.960

Table 3: Poincaré mode properties

In the figure below the e-folding decay lengths are given for varying values of A_v*, divided by the maximum decay length per Poincaré mode for the complete range of values. This shows that (in general) the decay length increases with increasing viscosity, but that the variation is small (no more than 9% for a rate between 0.01 and 10). Some modes achieve a local maximum at a rate of about 0.5 and then decrease slightly to start increasing again for higher rates. That the influence of the Poincaré modes extends *further* when the viscosity increases seems a paradox, but apparently is a property of these modes. This can be observed in the wave number plot of figure Figure 6. For higher viscosity the real part of the wave number gets relatively higher (compared to the imaginary part), though it remains relatively small. But because this ratio changes its influence along the basin gets larger.

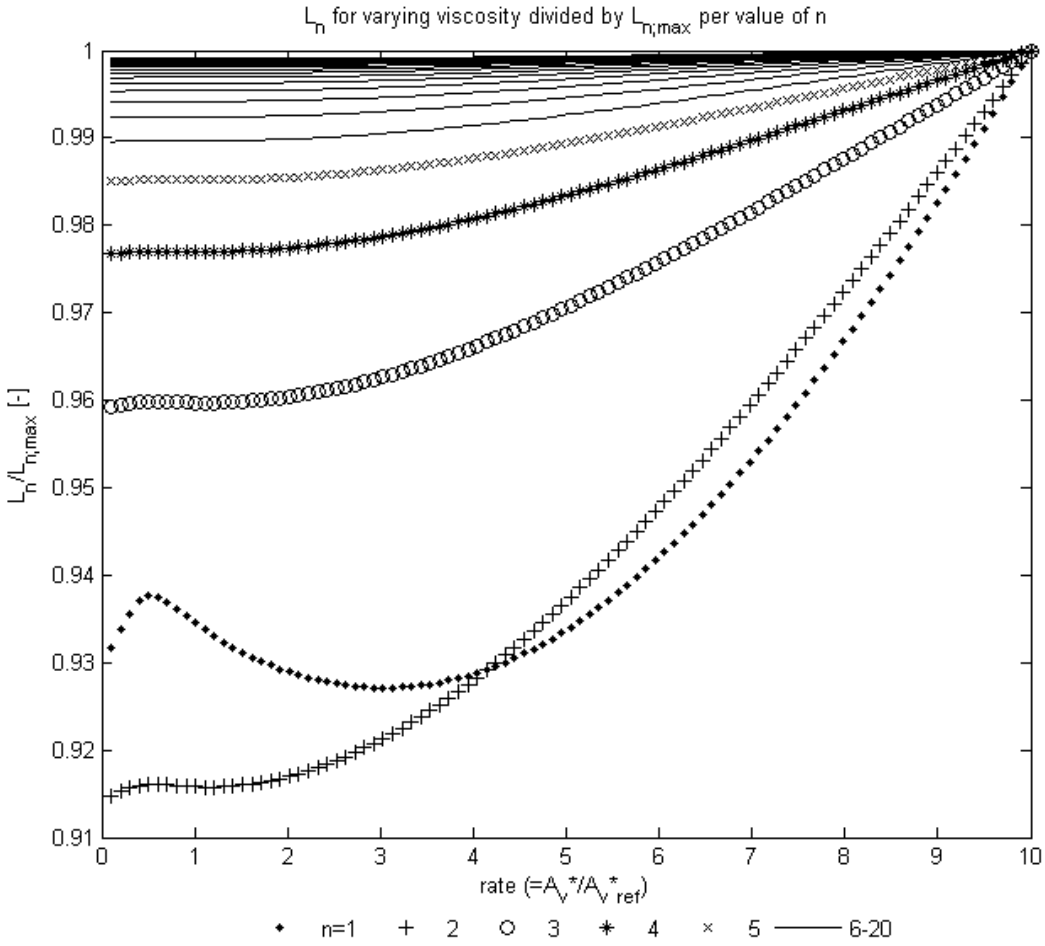

Figure 8: Poincaré decay length L_n for varying viscosity divided by $L_{n;max}$ per value of n

5.1.4 TRANSLATION OF WAVE MODE PROPERTIES TO 2DH FRICTION

The 2DH model presented by Rienecker & Teubner (1980) can be seen as a simplification of the 3D model presented here. The only difference is that their model is depth-averaged and therefore does not use a slip condition and has a friction term that is a parameterization of the friction term used here. This means that there is no viscosity parameter or slip parameter but a single friction parameter r_{fr}*. The question is which value for r_{fr}* should be chosen to approximate the 3D flow properties. A first simple approximation based on velocity properties is given by $r_{fr}^{*} = 8/(3p)C_d U^{*}$ [5.5] (the Lorentz linearization of a quadratic friction law, see Zimmerman 1982) which gives r_{fr}*=0.0012 m/s. This could be a reasonable approximation as it is directly based on the physical properties of the basin that still apply to the depth-integrated model.

Another way to find values for r_{fr}* is by trying to approximate the properties of the individual wave modes mentioned above. For this ranges of values for A_v* and s* are used to determine the Kelvin wave length λ (a), Kelvin dissipation factor D (b) and the e-folding decay-length of the first Poincare mode L_1 (c). These properties are also determined for a range of values of r_{fr}*. Per combination of A_v* and s* a value for r_{fr}* is then found which has the smallest absolute difference with respect to λ, D and L_1. These results can be observed in the plot below.

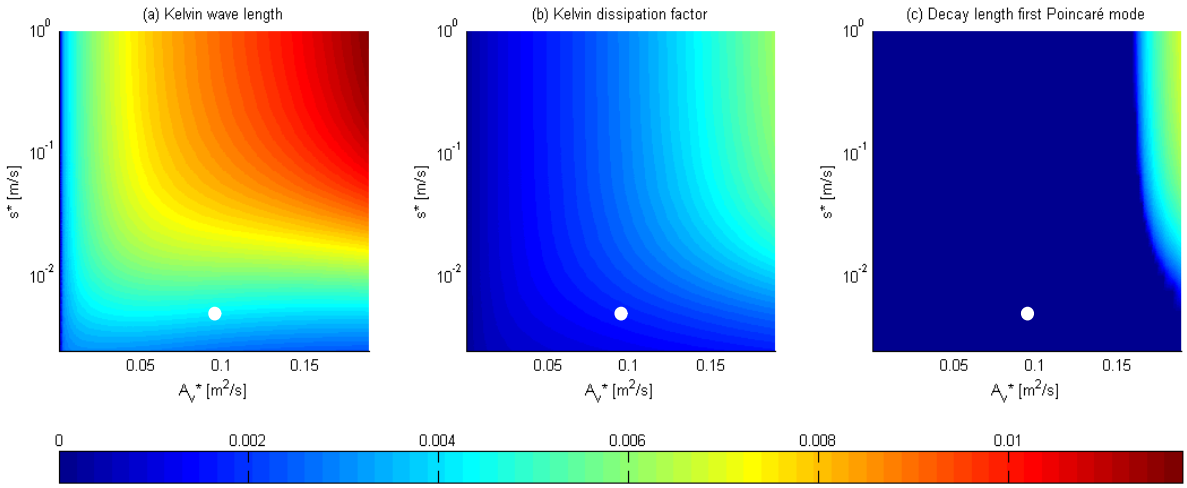

Figure 9: results for r_{fr}* [m/s] for combinations of A_v* and s* by fitting on (a) **λ***, (b) D* and (c) L_1*

It should be noted that the ranges chosen for A_v* and s* in the figure above are based on the range of typical values for the North Sea in Besio et al. (2008). This range was between 0.01 and 0.05 m^2/s, but was extended to between slightly above zero and almost 0.20 m^2/s (approximately 2 times $A_{v;ref}$*) to show something more of the development of r_{fr}*. The range reported for s* was between 0.005 and 0.01 m/s, but was extended to between slightly above zero and 1 m/s because the development of r_{fr}* below 0.01 m/s was quite minimal for the dissipation factor and decay length plot. It should also be noted that the horizontal scale is logarithmic.

In the figure above it can be seen that in general with increasing A_v* and s the friction parameter r_{fr}* becomes higher. This is because friction and viscosity both cause energy dissipation and because the slip parameter also limits the flow throughout the water column by limiting the flow at the bottom. The Kelvin wave length and dissipation factor plots show a continuous development of r_{fr}* which is to be expected as those parameters are closely related to dissipation effects.

For the decay length plot a large combination of slip and viscosity parameters lead to a value of zero for r_{fr}*. This means that only an inviscid depth-averaged Poincaré mode can approach the desired 3D decay length. This is probably because the imaginary part of the Poincaré wave number and thereby the decay length only lightly responds to changes in viscosity (see Figure 6 through Figure 7). Only with higher viscosities than about 0.15 m^2/s (about 1.4 times $A_{v;ref}$*) the decay length of the first Poincaré mode becomes lower than it was for zero viscosity (see Figure 8) and for somewhat higher values there is more development of r_{fr}* in the figure above. This means that the decay length is always lower for the 3D model until viscosity is high enough (largely regardless of s*).

With the reference case mentioned in the introduction of this chapter it is found that r_{fr}* equals $4.1*10^{-3}$, $1.7*10^{-3}$ and 0 m/s for the fitting parameters (a), (b) and (c) respectively. Even the largest of these values is still a factor 3 smaller than that found with expression [5.5] and the three fitted values themselves also differ significantly; this at least signifies that the 4 methods are distinct, which leads to the best results depends on what is deemed most important. In the following paragraphs and chapters this is explored further.

5.2 PROPERTIES OF THE TOTAL SOLUTION

In this chapter properties of the total solution are given in the form of elevation and current amphidromic systems. The solution is constructed by use of the collocation method described in paragraph 4.3; this method determines the relative amplitudes (R for the outgoing Kelvin wave and η_n for all used Poincaré modes) in such a way that there is no depth-averaged normal flow at the

lateral boundary. The amphidromic systems are compared to an equivalent depth-averaged model with the values for r_{fr}* derived before.

In general the amplitude is determined by removing the time-dependent component of the expression (for u, v, w or η) and taking the absolute value (complex modulus). This gives an expression that gives the amplitude per x,y-location. This can be seen in the expression below for the fictional parameter p (which can be replaced with u, v, w or η).

$$r_{p;total}(x,y) = \left| p_0(-x, B-y) + Rp_0(x,y) + \sum_{n=1}^{N} p_n(x,y) \right| \qquad [5.6]$$

Instead of taking the absolute value also the phase can be determined which yields the following expression. Coordinates with the same phase reach their maximum value at the same moment in the tidal period.

$$q_{p;total}(x,y) = \arg\left(p_0(-x, B-y) + Rp_0(x,y) + \sum_{n=1}^{N} p_n(x,y) \right) \qquad [5.7]$$

5.2.1 Elevation amphidromic system of the total solution

In the figure below the elevation amphidromic system is given; in this figure the coloured lines signify the contours of a certain tidal elevation in m while the black lines denote the phase at which that point reaches its highest elevation. In general this tidal pattern looks like what can be expected in a semi-enclosed basin.

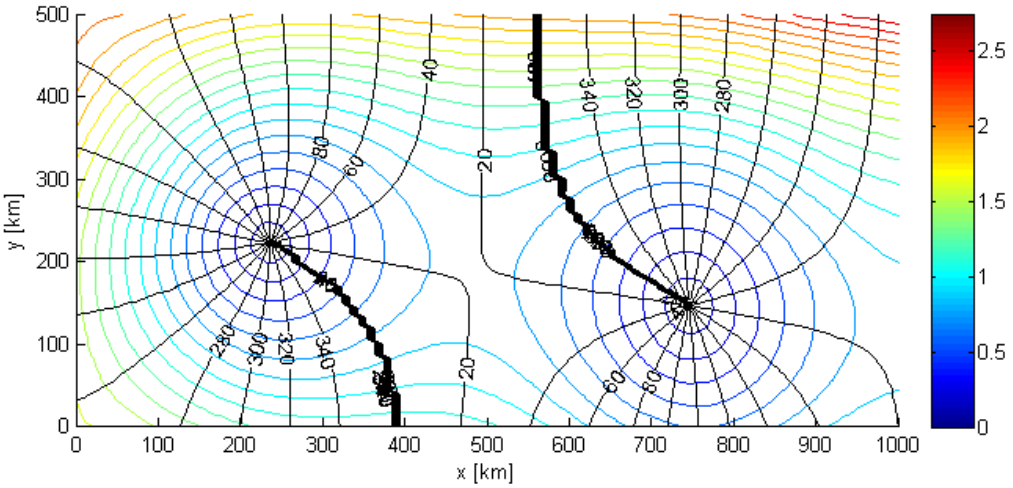

Figure 10: amplitude and phase of **η** [m]

The one produced by Davies and Jones (1995) looks similar. The phase pattern has a similar shape but has a phase shift of about 300 degrees. The amphidromic points (where the amplitude is zero) lie at roughly the same location and the amplitude development looks very similar as well. This strengthens the trust in performance of the model as those authors used a more complex numerical 3D model. In the following plots the elevation amphidromic system of the basin is plotted for the depth-averaged model. For this the four values of r_{fr}* derived in paragraph 5.1.4 are used.

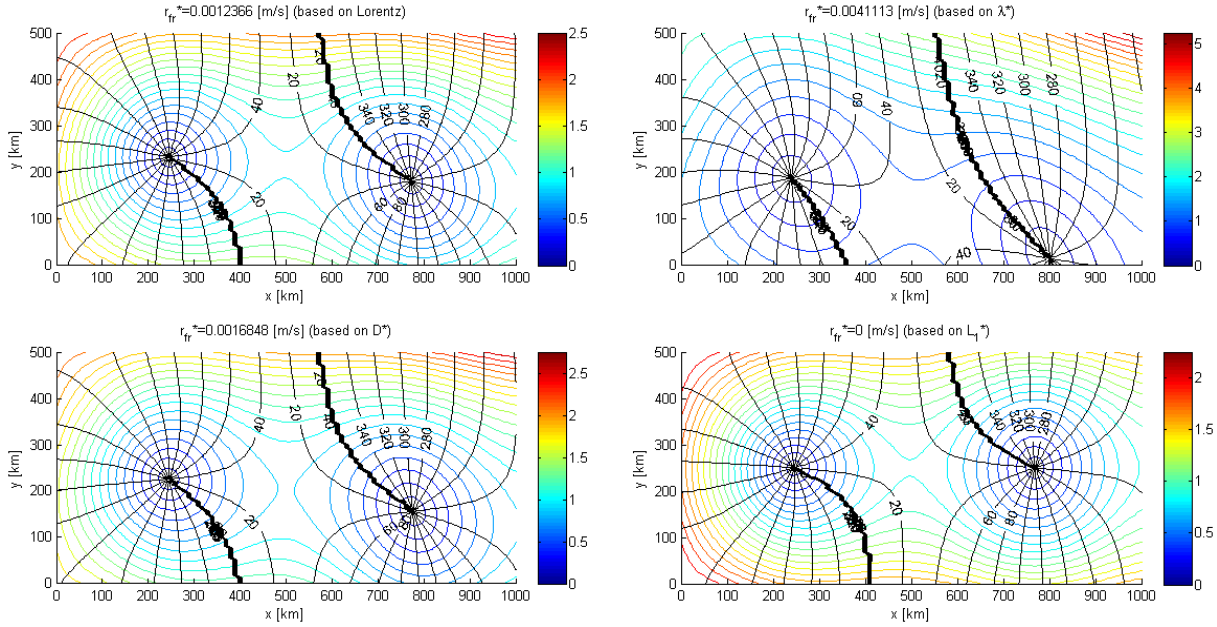

Figure 11: amplitude and phase of **η** [m] in the depth-averaged model

From the amphidromic plots it can be seen that the depth-averaged model has widely differing results for the four values of r_{fr}*. Those found with the Lorentz linearization and Kelvin dissipation factor D come rather close, but those based on the Kelvin wave length and the first Poincaré decay length do not. It should be noted that the approach with the largest friction (based on Kelvin wave length) gets the highest amplitudes because the amplitude of the elevation (and velocities) of the incoming Kelvin wave is fixed at the lateral coast for all variants and increases with distance from the lateral coast. Because friction is high, the decrease when moving *towards* the boundary is large and therefore the increase when moving *away from* the boundary is large. Therefore the amplitudes near the upper coast and the basin entrance (where the influence of the incoming Kelvin wave is strongest) become very large.

Plots of the elevation amphidromy for varying viscosity and slip parameter are found in appendix D.

5.2.2 LONGITUDINAL CURRENT AMPHIDROMIC SYSTEM

In the figure below the longitudinal current amphidromic system is given (at the bottom). This shows that the current amphidromic points are localized between the elevation amphidromic points, which is because the elevation gradients are minimal there and the velocities must become very small as well (this relation derives from the governing equations).

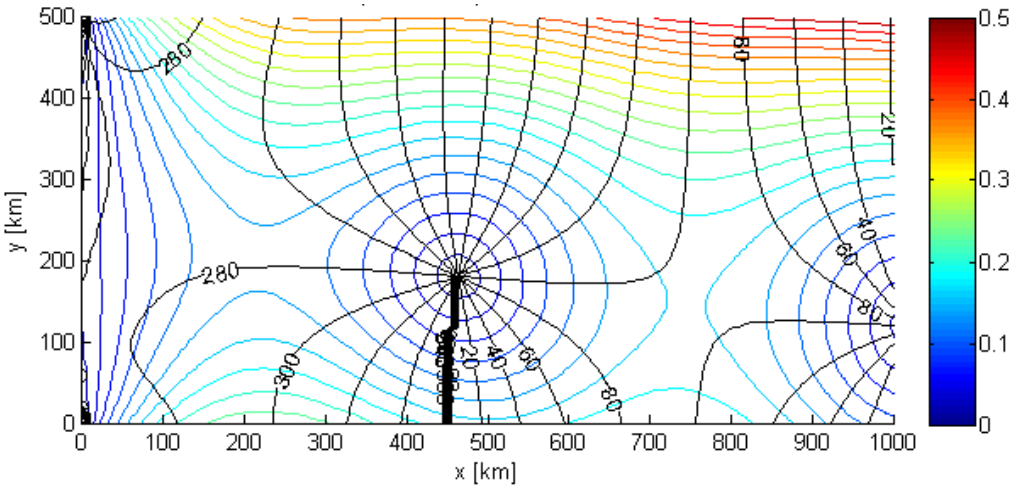

Figure 12: amplitude and phase of u [m/s] (at the bottom)

In the following plots the longitudinal current amphidromic system of the basin is plotted for the depth-averaged model with values for r_{fr}* as found before.

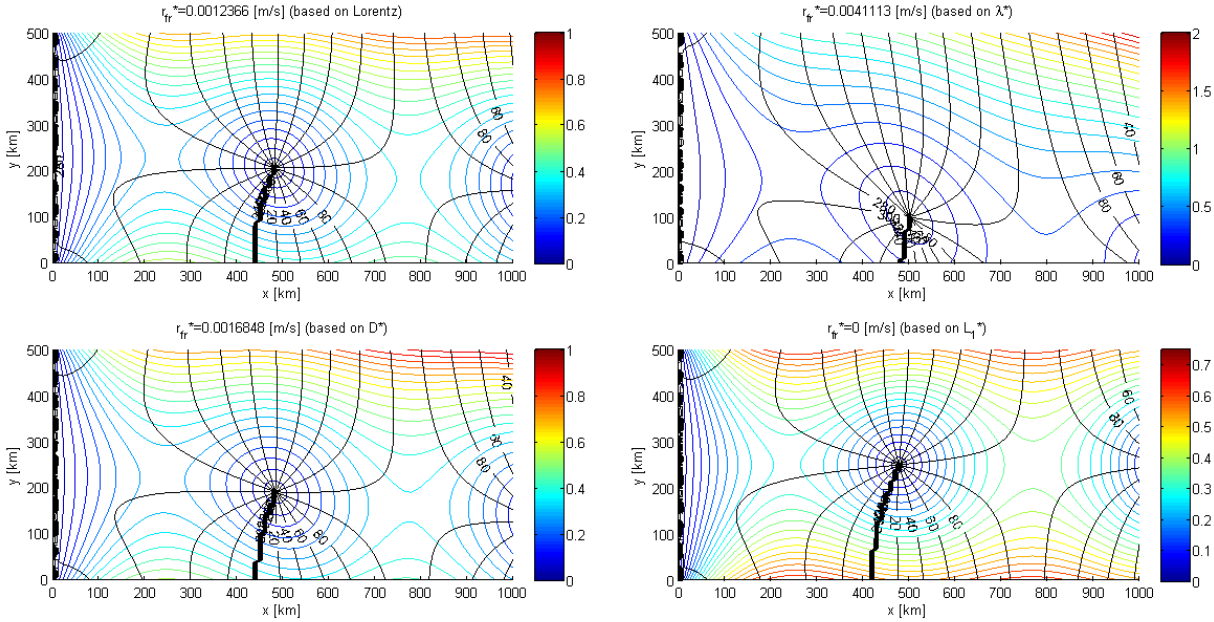

Figure 13: amplitude and phase of u in the depth-averaged model

This shows a similar comparison of 3D and 2DH as for elevation. Again the approaches based on Kelvin dissipation and Lorentz linearization perform best.

To compare the 3D approach with the 2DH approach the amplitude and phase across the water column at x*=354 km and y*=244km are plotted below. This location was chosen because no amphidromic point appears there and the figures are just meant to illustrate the differences between 3D and 2DH for a 'neutral' location.

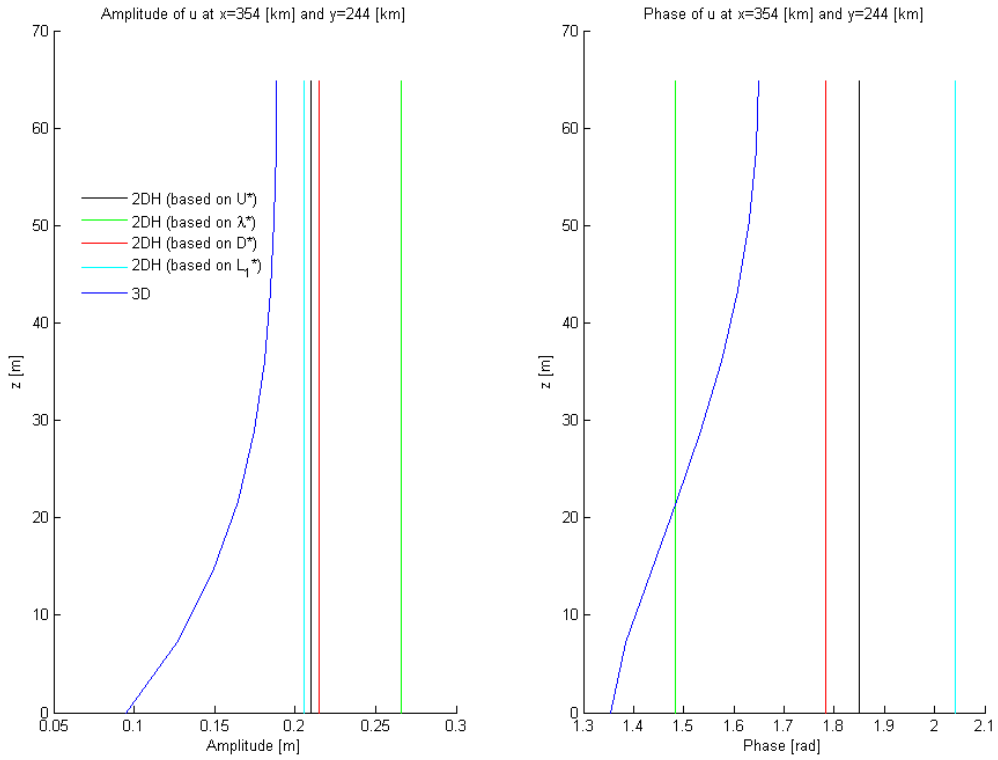

Figure 14: comparison of amplitude and phase of u across the channel

This figure shows that there is a clear phase and amplitude difference between the 2DH and 3D approaches, but also along the vertical for the 3D approach as well. This signifies the importance of a 3D approach in determining the precise structure of flow.

5.2.3 LATERAL CURRENT AMPHIDROMIC SYSTEM

In the figure below the lateral current amphidromic system is given (at the bottom). The amphidromic points are very different from those of the longitudinal current system and it can be seen that the influence of the Poincaré modes (which appear mostly in the left part of the basin) is stronger than that of the Kelvin waves (which dominate in the right part of the basin).

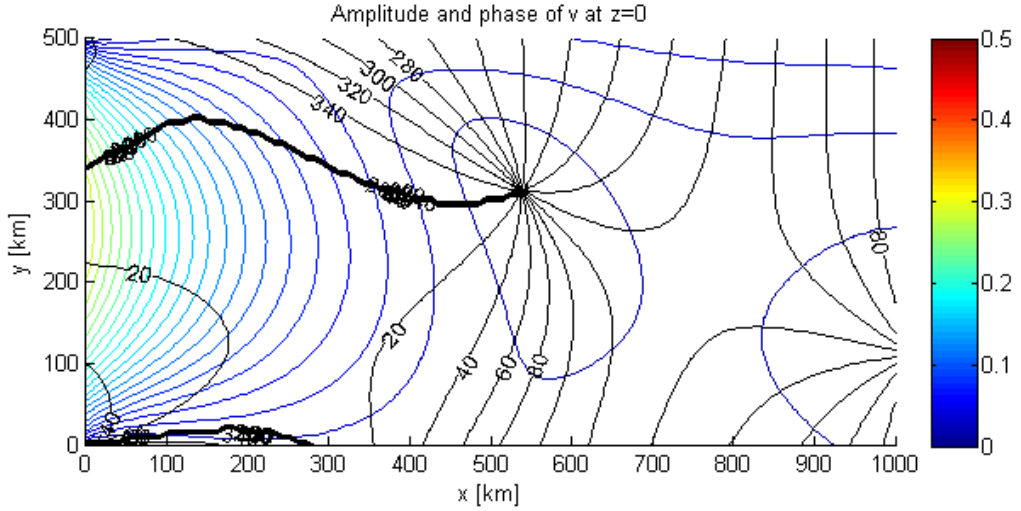

Figure 15: amplitude and phase of v (at the bottom)

6 BOTTOM SHEAR STRESS MODELLING IN A SEMI-ENCLOSED BASIN

In this chapter bottom shear stress is calculated for the 3D model as well as the 2DH model (with the values for r_{fr}* found before). After that better values for the friction parameter are sought by fitting the bottom shear stress amphidromy of 2DH to that of the 3D case by adjusting the friction parameter.

6.1 BOTTOM SHEAR STRESSES OF THE 3D MODEL

To calculate the horizontal bottom shear stress the following formula is applied; $\vec{t}^{\,*}_b = \left(t^*_{b;x}, t^*_{b;y}\right) = s^*\left(u^*_{total}\big|_{z=0}, v^*_{total}\big|_{z=0}\right)$ [6.1]. The amphidromic plot of these bottom shear stresses can be seen below.

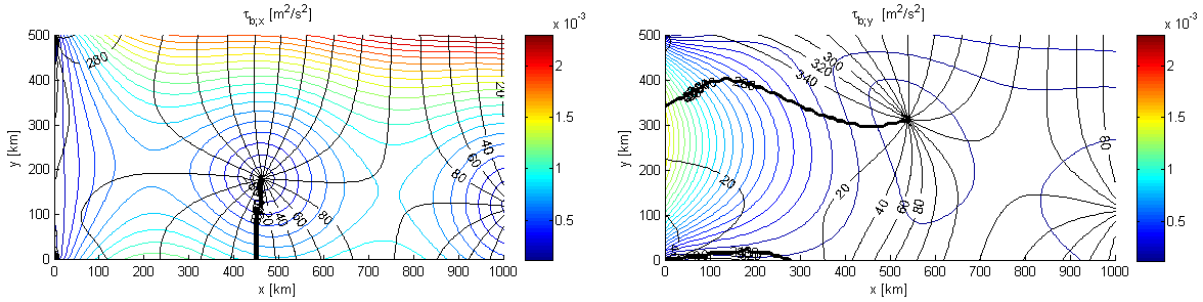

Figure 16: bottom shear stress (m^2/s^2) amphidromy in horizontal direction (3D model)

These plots of course have the same shape as the horizontal velocity plots of before. Only the values differ with a factor of s*. In analogy to the velocity plots it is observed that the stresses in x-direction are greater than those in the y-direction in the majority of the basin. Only at the lateral boundary the lateral stresses are greater, because there the longitudinal velocity at the bottom is limited by the boundary condition that there can be no normal depth-integrated longitudinal velocity at the boundary. The shear stresses in the lateral direction are probably largely dominated by the Poincaré modes, given the pattern. Because the influence of the lateral shear stress is generally limited throughout the basin it is not taken into account in the following comparison with the depth-averaged model.

6.2 BOTTOM SHEAR STRESSES OF THE DEPTH-AVERAGED MODEL

To find out how the results of the 3D case compare with the 2DH case shear stress is also calculated with the depth-averaged model. Herein it is assumed that the resulting velocities apply at the water bottom. The shear stress is then calculated with $\vec{t}^{\,*}\big|_{2DH} = \left(t^*_x\big|_{2DH}, t^*_y\big|_{2DH}\right) = r^*_{fr}\left(\left\langle u^*_{2DH}\right\rangle, \left\langle v^*_{2DH}\right\rangle\right)$ [6.2]. This leads to the following results (with the values for r_{fr}* found before).

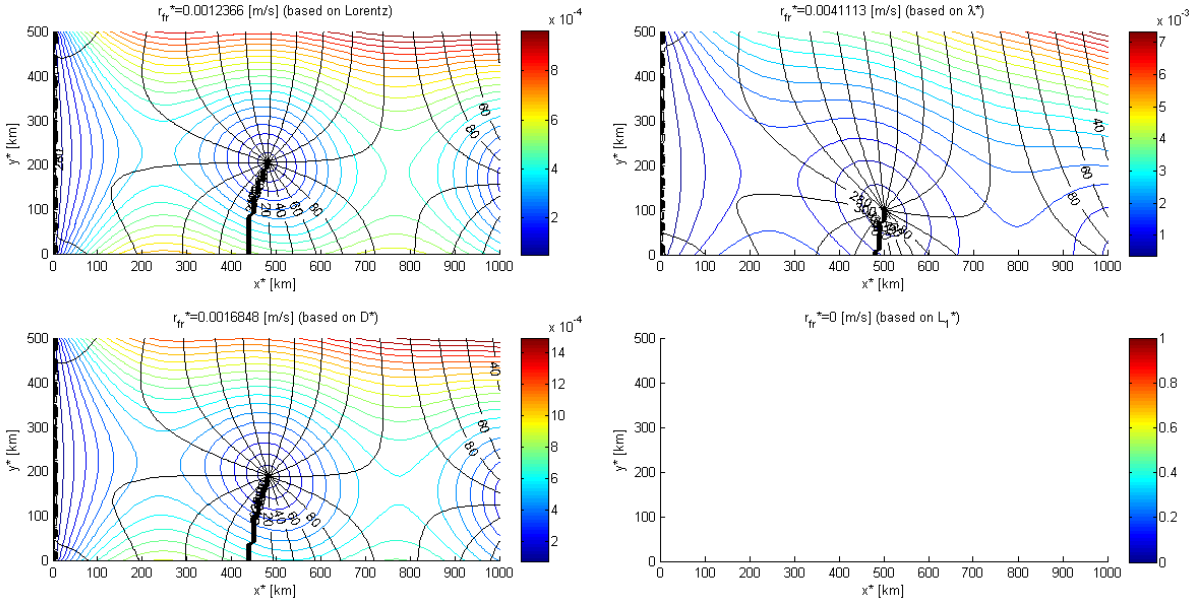

Figure 17: 2DH shear stress amphidromy in x-direction fitted on Lorentz and wave mode properties

In the figure above it can be seen that the shear stresses of the 2DH model differ little to a lot with those of the 3D model. The r_{fr}* based on Lorentz leads to 3 times too low amplitudes, r_{fr}* based on the Kelvin wave length leads to 3 times too high amplitudes, r_{fr}* based on the Kelvin dissipation factor leads to about 1.3 times too low amplitudes and r_{fr}* based on the first Poincaré decay length gives no shear stress at all (because r_{fr}*=0, see [6.2]). In general the 2DH model is weak in correctly predicting shear stresses, though the approach based on dissipation factor D* gives a reasonable result.

6.3 VALIDITY OF 2DH BOTTOM SHEAR STRESSES

To check how well the different 2DH approaches match the 3D shear stresses a *basin error function* is defined. This function is shown in the following expression:

$$BE_{avg} = \left[\frac{1}{B^* L^*} \int\int \left(t^*_x \big|_{2DH} - t^*_{x;b} \big|_{3D} \right)^2 dx^* dy^* \right]^{1/2}. \qquad [6.3]$$

Here L* is the plotting domain used before, which is somewhat smaller than the 3D Kelvin wave length for the reference case (see paragraph 5.1.2). The integral is taken over the entire plotting domain, though it is solved numerically rather than analytically. To have some references values to compare with the 2DH results of individual wave modes expression [6.3] for the bottom shear stresses of the full 2DH Taylor solution is minimized by finding the best fitting value for r_{fr}*. Because previous results seem to signify that the Kelvin dissipation factor is a good measure of the full solutions shear stresses the same is also done for just the incoming 2DH Kelvin wave (which is of course compared with the shear stresses caused by the incoming 3D Kelvin wave). It should be noted that both results are just used as references; they serve as a kind theoretical best match between 2DH and 3D bottom shear stresses. The results of these two optimizations can be seen in the figure below.

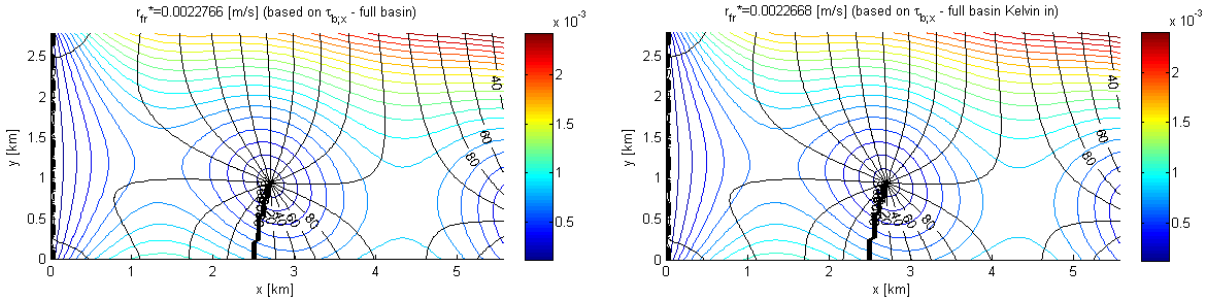

Figure 18: 2DH shear stress (m^2/s^2) amphidromy in x-direction fitted on bottom shear stress

In the figure above it can be seen that both methods lead to similar results. The values found for r_{fr}* differ less than 1% and the amphidromic patterns are almost indistinguishable. This means that by just looking at the incoming Kelvin wave values for r_{fr}* can be found that comes very close to the one found when looking at the full Taylor solution. The stresses also compare well to the bottom shear stresses in x-direction as calculated for the 3D model (see Figure 16). The resulting individual wave mode properties of the 4 2DH approximations, the 2 2DH basin error function optimizations and the 3D model are presented below. Also the maximum amplitude calculated for the basin (absolute and as a percentage of the 3D maximum amplitude) and the value for BE_{avg} are given (absolute and as a percentage of the 3D maximum amplitude).

Based on	r* [m/s]	**λ*** [km]	D* [-]	L1* [km]	Max $\|\tau_{b;x}\|$ [m2/s2]	Max $\|\tau_{b;x}\|$ [%]	BE_{avg} [m2/s2]	BE_{avg} [%]
Lorentz	1.24E-03	1126	0.65	180	1.01E-03	42	5.14E-04	21
λ*	4.11E-03	1102	0.26	179	7.71E-03	319	1.39E-03	58
D*	1.68E-03	1124	0.56	180	1.57E-03	65	3.17E-04	13
L_1*	0	1129	1.0	180	0	0	9.78E-04	40
Kelvin in	2.27E-03	1120	0.46	180	2.52E-03	104	7.45E-05	3
Taylor solution	2.28E-03	1120	0.46	180	2.54E-03	105	7.42E-05	3
3D	-	1102	0.56	181	2.41E-03	100	-	-

Table 4: summary of results of various methods

The table clearly shows that the two references cases derived in this paragraph work best (as expected, as they are meant to do just that) and also by themselves they work quite well (an average error throughout the basin of 3%). Also, the difference between the one based on the full Taylor solution and just the incoming Kelvin wave is very small. This further signifies that the incoming Kelvin wave is a very important measure of the full solution. An explanation for this is that the incoming Kelvin wave itself of course determines how the outgoing Kelvin wave Poincaré modes turn out. The information of that incoming wave therefore strongly determines the total solution.

Furthermore the quality of the Kelvin dissipation factor approach is once again confirmed. Its error is significant but still reasonable (13%) and all individual wave mode properties correspond well with the 3D case. After that the Lorent linearization gives the best result (21%), followed from afar by the Poincaré decay length approach (40%) and Kelvin wave length approach (58%). It should however be noted that the decay length approach in itself is very weak, as it defaults to a value of r_{fr}*=0 m/s in a lot of cases (see 5.1.4). Its meaning is therefore virtually non-existent, which is confirmed by the fact that it cannot even exactly approach the parameter it was based on in the first place! It does have the best fit (the numbers are rounded down), but it does not have an exact fit for its own parameter like the wave length and dissipation factor approaches do have.

7 DISCUSSION

The model presented in this paper has certain smaller and greater drawbacks. The chosen approach can only be applied to flat bottoms, while the influence of a sloping bottom can be significant (Davies & Jones, 1995). As there is no way to implement this in an analytical model this cannot be easily fixed. However, the model presented still leads to expected tidal behaviour so this may not be a big problem in this case. This also signifies that the assumptions (idealized basin shape, long waves et cetera) underlying the derivation of the linear governing equations and boundary conditions (starting from the Navier-Stokes equations) were reasonable for tidal flow in a semi-enclosed basin.

It could be argued that the turbulence model is too simple, though it is still an improvement compared to Mofjeld's work (1980). No variation of viscosity is allowed while that does occur. But still, the turbulence model at least gives 3D information and can be further tweak by adjusting the slip parameter so it is probably the best possible for an analytical model.

The models performance with other tidal constituents is unfortunately unknown. Also the validity of some parameters and especially the used reference slip parameter is unknown and may be relatively weak. This is one of the reasons it was not compared in great detail to more complex models or compared at all to actual basins.

It was assumed that a limited number of Poincaré modes would still lead to good results. For the reference case a truncated set of 20 Poincaré modes was used. In appendix E the relative amplitudes of the outgoing Kelvin wave and Poincaré modes of the 3D and 2DH model can be found. This shows that the higher Poincaré modes have a very small contribution compared to the lower Poincaré modes, which makes the use of a small set of Poincaré modes reasonable.

Furthermore this model was developed under the assumption that the Froude number is very small. For the used reference case the Froude number turns out to be 0.02 (with η_0*=1.5 m and H*=65m), so that assumption was reasonable.

Also it was assumed that only long waves are dealt with. As the Kelvin wave length turns out to be larger than 1000 km and the tidal elevation is 1.5 m this assumption was very reasonable.

8 CONCLUSION AND RECOMMENDATIONS

8.1 CONCLUSION

New expressions have been derived for the 3D flow field of a Kelvin wave experiencing vertical eddy viscosity in an infinite channel of finite width with a partial slip condition at the bottom. With these expressions the entire flow field can be calculated, which means the first research question is answered. The properties of that Kelvin wave have been investigated by delving into the expressions and the underlying parameters (wave number, et cetera). The Kelvin wave in general behaves as expected; it experiences increased dissipation with increased viscosity and has no depth-integrated lateral flow. One unexpected result was that though the Kelvin wave in general has *decreasing* wave length with increasing viscosity it still shows *increasing* wave length sometimes. This suggests its propagating character is increasing instead of decreasing. However, it should be noted that because of more rapidly increasing dissipation the net effect is still that it experiences increasing dissipation.

Mofjeld's (1980) analysis and the approach documented by Pedlosky (1982) were extended and indeed Poincaré modes were found to describe tidal flow in an infinite channel of finite width. For this new expressions were derived which eventually led to a condition (found by coupling the dispersion relation and near-coastal boundary condition) that allowed Poincaré modes. By using a partial-slip condition instead of a no-slip condition as done by the two mentioned authors the solution changed with respect to the parameters that describe the vertical dependency; this holds for the Kelvin waves as well as the Poincaré modes. This can easily be transformed back to the expressions for no-slip when the slip-parameter is set to infinity. The Poincaré modes also experience dissipation and are only active in a limited part of the basin. These modes do contribute to the depth-integrated lateral flow. Higher Poincaré modes decay over a shorter distance, but increasing viscosity leads to *greater* decay lengths.

By fitting the individual wave mode properties (Kelvin wave length, Kelvin dissipation factor and the first Poincaré decay length) of a depth-averaged model to those found for the 3D model values for friction parameters were found for ranges of viscosity and slip parameter values. This was applied to a reference basin (the North Sea) to find three specific friction parameters for further analysis. Also a value for the friction parameter was calculated from Lorentz linearization of the linear friction law. These were used in the depth-averaged model to compare a 3D approach with a 2DH approach.

By using a collocation method the Kelvin and Poincaré modes were combined to simulate tidal flow in a semi-enclosed basin. This method calculates the amplitudes of the outgoing Kelvin wave and Poincaré modes so that no depth-integrated normal flow is present at the lateral boundary. This quasi-analytical solution compares well to the numerical model results of Davies & Jones (1995). Between the 3D and 2DH version of the model there are significant differences in amplitude of the elevation and currents. This signifies the importance of a 3D approach. This means that (as expected) for correct shear stress calculations a 3D approach is more appropriate as stress depends on the current properties.

However, it is possible to approximate the shear stresses of the 3D model with a 2DH model reasonably well. A theoretically lowest average error of 3% was found by fitting the entire shear stress pattern as a reference. The friction parameter found with the Kelvin dissipation factor lead to an error of 13% (r_{fr}* was about $1.7*10^{-3}$), while the one found with the Lorentz linearization lead to an error of 21% (r_{fr}* was about $1.2*10^{-3}$). This is a promising result that can be improved further with the use or inclusion of more parameters. Especially parameters that relate to the (dissipation of) the incoming Kelvin wave will be of great relevance.

All in all the construction of the first analytical 3D-model that describes tidal flow in a semi-enclosed basin using Kelvin and Poincaré modes with partial slip has lead to a valuable and promising instrument in further improving 3D and 2DH modelling.

8.2 RECOMMENDATIONS

Although the model seems to perform well, it can be further validated by doing more sensitivity checks and more comparison with the mentioned and other authors. For instance Mofjeld (1980) describes more properties of the found Kelvin wave, such as the behaviour of the co-phase lines under influence of changing tidal frequency. Furthermore the behaviour in the boundary layers, the effects of a changing slip parameter on the individual wave modes and the tidal ellipses can be studied. The influence of the amplitude of the tidal elevation at the open end relative to the maximum depth and the influence of basin dimensions is found to be important by Winant (2007). Also the ability of the model to correctly include viscous effects can be checked by investigating if it reproduces the anticlockwise component of flow (Davies & Jones, 1995). This all was not done in this research because it was outside the initial scope and could not be investigated quickly to add it later.

Some properties that were investigated can be studied more thoroughly. For instance it is interesting to check how the (current) amphidromic plots change when amongst others the viscosity and tidal frequency (i.e. different tidal constituents) are adjusted. Also the lateral bottom shear stresses, tidally averaged bottom shear stresses can be of interest as well as the (dominant) direction of these stresses.

A possible weakness of the model is its greatly idealized basin shape and parameters that are assumed to be constant (e.g. the eddy viscosity). It is therefore advised to investigate how important these aspects are for this particular model. This can be done by (as mentioned before) checking it with more other models, but also by trying to simulate basins that are closer (Gulf of California, see Carbajal & Backhaus, 1997) or further removed from the idealized basin shape. Also it is recommended to find better values for certain parameters, especially the slip parameter.

The quasi-analytical approach also allows for the coupling of separate semi-enclosed basins with different dimensions and parameters. Coupling the Northern part (Davies & Jones, 1995) with the Southern Bight (Roos & Schuttelaars, 2009) is possible and may lead to interesting results. If this works out well the models applicability greatly increases. It may also be possible to couple a semi-enclosed basin like an estuary with a single-coast basin like a shelf sea as done by Ye & Garvine (1998), but that requires some extra work for the single-coast basin as that is not supported by the current version of the model.

The translation of 3D properties to a well-performing 2DH model can be further improved. It follows from the analysis presented here that the Kelvin wave and especially the Kelvin dissipation are a good measure of the total 3D solution. Other parameters that say something about the Kelvin wave could be used as the dissipation factor has been in this study to find a well-fitting friction parameter. For instance the amplitude of bottom shear stress at the lateral boundary could be used or the Rossby deformation radius. Maybe a combination of different parameters (dissipation factor combined with bottom shear stress amplitude) in a mixed fitting algorithm can lead to even better results. Especially in shallower basins or with greatly veering flow it is recommended to also include the lateral bottom shear stress in the analysis as that will increase in magnitude.

LITERATURE

BESIO, G. (2008), P. BLONDEAUX, M. BROCCHINI, S.J.M.H. HULSCHER, D. IDIER, M.A.F. KNAAPEN, A.A. NÉMETH, P.C. ROOS & G. VITTORI. The morphodynamics of tidal sand waves: A model overview. *Coastal Engineering* (Vol. 55, No. 7-8), pp. 657-670.

BOWDEN, K.F. (1967). Turbulent mixing in tidal currents. *The Physics of Fluids* (10), pp. S278-S280.

BOWDEN, K.F. (1978). Physical problems of the benthic boundary layer. *Geophysical Surveys* (3), pp. 255-296.

CARBAJAL, N. & BACKHAUS, J.O. (1997). Simulation of tides, residual flow and energy budget in the Gulf of California. *Oceanologica Acta* (21, No. 3), pp. 429-446.

DANIELSON, S. & KOWALIK, Z. (2005). Tidal currents in the St. Lawrence Island region. *Journal of Geophysical Research* (110).

DAVIES, A.M. & JONES, J.E. (1995). The influence of bottom and internal friction upon tidal currents: Taylor's problem in three dimensions. *Continental Shelf Research* (15, No. 10), pp. 1251-1285.

GERKEMA, T. (2000). A linear stability analysis of tidally generated sand waves. *Journal of Fluid Mechanics* (417), pp. 302-322.

HENDERSHOTT, M.C. & SPERANZA, A. (1971). Co-oscillating tides in long, narrow bays; the Taylor problem revisited. *Deep-Sea Research* (18), pp. 959-980.

HUIJTS, K.M.H. (2009), SCHUTTELAARS, H.M., DE SWART, H.E. & FRIEDRICHS, C.T. Analytical study of the transverse distribution of along-channel and transverse residual flows in tidal estuaries. *Continental Shelf Research* (29), pp. 89–100.

HULSCHER, S.J.M.H. (1996). Tidal-induced large-scale regular bed form patterns in a three-dimensional shallow water model. *Journal of Geophysical Research* (101, No. C9), pp. 20,727-20,744.

HULSCHER, S.J.M.H. & VAN DEN BRINK, G.M. (2001). Comparison between predicted and observed sand waves and sand banks in the North Sea. *Journal of Geophysical Research* (106, No. C5), pp. 9327, 9338.

IANNIELLO J.P. (1981). Tidally-induced Residual Currents in Long Island and Block Island Sounds. *Estuarine, Coastal and Shelf Science* (12), pp. 177-191.

MOFJELD, H.O. (1980). Effect of vertical viscosity on Kelvin waves. *Journal of Physical Oceanography* (10), pp. 1039-1050.

PEDLOSKY, J. (1982). *Geophysical Fluid Dynamics.* New York: Springer-Verlag.

PRANDLE, D. (1982). The vertical structure of tidal currents and other oscillatory flows. *Continental Shelf Research* (1, No. 2), pp. 181-207.

PRANDLE, D. (1997). The influence of bed friction and vertical eddy viscosity on tidal propagation. *Continental Shelf Research* (17, No. 11), pp. 1367-1374.

RIENECKER, M.M. & TEUBNER, M.D. (1980). A note on frictional effects in Taylor's problem. *Journal of Marine Research* (38), pp. 183-191.

ROOS, P.C. & SCHUTTELAARS M. (2009, ACCEPTED). Solving the viscous Taylor problem. *Journal of Fluid Mechanics*.

SINHA, B. & PINGREE R.D. (1997). The principal lunar semidiurnal tide and its harmonics: baseline solutions for M2 and M4 constituents on the North-West European Continental Shelf. *Continental Shelf Research* (17, No. 11), pp. 1321-1365.

SWART, H.E. DE (2008). Ocean waves. *Lecture Notes*.

TAYLOR, G.I. (1921). Tidal oscillations in gulfs and rectangular basins. *Proceedings of the London Mathematical Society* (20), pp. 148-181.

TEE, K-T. (1982). The Structure of Three-dimensional Tide-generating Currents: Experimental Verification of a Theoretical Model. *Estuarine, Coastal and Shelf Science* (14), pp. 27-48.

WINANT, C.D. (2007). Three-dimensional tidal flow in an elongated, rotating basin. *Journal of Physical Oceanography.* (37), pp. 2345-2362.

YE, J. & GARVINE R.W. (1998). A model study of estuary and shelf tidally driven circulation. *Continental Shelf Research* (18), pp. 1125-1155.

ZIMMERMAN, J.T.F. (1982). On the Lorentz linearization of a quadratically damped forced oscillator. *Physics Letters A* (89, No. 3), pp. 123-124.

LIST OF SYMBOLS

The symbols used in the main text of this thesis and their meaning can be found below.

Scaled	Dimensional	Units	Meaning
A	-	-	amplitude of depth-averaged velocity at the coast
	A_h*	m^2/s	horizontal eddy viscosity
	A_v*	m^2/s	vertical eddy viscosity
B	B*	m	basin width
	BE_{avg}*		average error throughout basins between 3D and 2DH
	C_D	-	viscosity coefficient
	f*	s^{-1}	Coriolis parameter / ration of inertial and tidal frequency
	g*	m/s^2	gravitational constant
H	H*	m	undisturbed water depth
H_e	-	-	correction on 1 incorporating vertical structure (see γ)
	K*	m^{-1}	typical inviscid Kelvin wave number
k_0	-	-	Kelvin wave number
k_n	-	-	Poincaré wave number
L	L*	m	basin length
m	-	-	collocation number
n	-	-	Poincaré number
N	-	-	used number of Poincaré modes
q	-	-	clockwise rotating velocity component
Q	-	-	clockwise rotating depth-dependence of elevation
r	-	-	counter clockwise rotating velocity component
R	-	-	counter clockwise rotating depth-dependence of elevation
r_{fr}	r_{fr}*	m/s	2DH friction parameter
r_p	-	-	amplitude of placeholder parameter p (replaceable with u, v, w or η)
s^{-1}	s*	m/s	ratio of slip and vertical viscosity parameter / slip parameter
t	t*	s	time
u	u*	m/s	alongshore horizontal velocity
	U*	m/s	typical inviscid Kelvin velocity
v	v*	m/s	lateral horizontal velocity
w	w*	m/s	upwards vertical velocity
	W*	m/s	vertical velocity scale
x	x*	m	alongshore horizontal coordinate
y	y*	m	lateral horizontal coordinate
y_m		-	lateral collocation coordinates
z	z*	m	upwards vertical coordinate
$\overline{Z}$	-	-	clockwise rotating depth-dependence of horizontal velocity
$\hat{Z}$	-	-	counter clockwise rotating depth-dependence of horizontal velocity
$\tilde{Z}$	-	-	rotating depth-dependence of vertical velocity
α_0	-	-	Kelvin wave number root parameter
α_n	-	-	Poincaré wave number root parameter
α_q	-	-	clockwise rotating root parameter
α_r	-	-	counter clockwise rotating root parameter
γ	-	-	correction on f incorporating vertical structure (see H_e)
δ_h	-	-	ratio of horizontal boundary layer and typical inviscid Kelvin wave length

δ_v	-	-	square of Stokes number
ε	-	-	Froude number
η	η*	m	sea level elevation
$\overline{h}$	-	-	lateral dependence of elevation amplitude
$\hat{h}$	-	-	lateral dependence of Poincaré velocity amplitude
	η_0*	m	elevation amplitude factor
	θ*	°	latitude
θ_p	-	-	phase of placeholder parameter p (replaceable with u, v, w or η)
	σ*	s^{-1}	tidal frequency
	Ω*	s^{-1}	angular frequency of the Earth's rotation

Table 5: symbols used in this thesis

APPENDICES

A. MODIFYING THE NAVIER-STOKES EQUATIONS AND BOUNDARY CONDITIONS

It is assumed that the flow is incompressible. Therefore the continuity equation reduces to the following because density ρ* now is constant, the density derivative becomes zero and the density parameter can be divided from the original equation:

$$u^*_{x^*} + v^*_{y^*} + w^*_{z^*} = 0\,. \qquad \text{[App.1]}$$

Incompressible flow coupled with the assumption of constant dynamic viscosity μ and gravity makes that the momentum equations reduce to the following:

$$r^*\left(u^*_{t^*} + u^*u^*_{x^*} + v^*u^*_{y^*} + w^*u^*_{z^*}\right) = -p^*_{x^*} + m^*\left(u^*_{x^*x^*} + u^*_{y^*y^*} + u^*_{z^*z^*}\right), \qquad \text{[App.2]}$$

$$r^*\left(v^*_{t^*} + u^*v^*_{x^*} + v^*v^*_{y^*} + w^*v^*_{z^*}\right) = -p^*_{y^*} + m^*\left(v^*_{x^*x^*} + v^*_{y^*y^*} + v^*_{z^*z^*}\right), \qquad \text{[App.3]}$$

$$r^*\left(w^*_{t^*} + u^*w^*_{x^*} + v^*w^*_{y^*} + w^*w^*_{z^*}\right) = -p^*_{z^*} + m^*\left(w^*_{x^*x^*} + w^*_{y^*y^*} + w^*_{z^*z^*}\right). \qquad \text{[App.4]}$$

Because the water depth is small compared to tidal wave length (long waves) vertical velocity w is relatively small, as are its derivatives and the momentum equation for w reduces to the following:

$$r^*g^* = p^*_{z^*} \rightarrow p^* = r^*g^*\left(H^* + h^*\right), \qquad \text{[App.5]}$$

which is the expression for hydrostatic pressure. This can be put back in the momentum equations for u* and v* to find the following (H* drops from the equation because its derivative is zero):

$$r^*\left(u^*_{t^*} + u^*u^*_{x^*} + v^*u^*_{y^*} + w^*u^*_{z^*}\right) = -r^*g^*h^*_{x^*} + m^*\left(u^*_{x^*x^*} + u^*_{y^*y^*} + u^*_{z^*z^*}\right), \qquad \text{[App.6]}$$

$$r^*\left(v^*_{t^*} + u^*v^*_{x^*} + v^*v^*_{y^*} + w^*v^*_{z^*}\right) = -r^*g^*h^*_{y^*} + m^*\left(v^*_{x^*x^*} + v^*_{y^*y^*} + v^*_{z^*z^*}\right). \qquad \text{[App.7]}$$

By dividing these equations with the density parameter and replacing μ*/ρ* with the kinematic viscosity A the following expressions are found:

$$\left(u^*_{t^*} + u^*u^*_{x^*} + v^*u^*_{y^*} + w^*u^*_{z^*}\right) = -g^*h^*_{x^*} + A^*\left(u^*_{x^*x^*} + u^*_{y^*y^*} + u^*_{z^*z^*}\right), \qquad \text{[App.8]}$$

$$\left(v^*_{t^*} + u^*v^*_{x^*} + v^*v^*_{y^*} + w^*v^*_{z^*}\right) = -g^*h^*_{y^*} + A^*\left(v^*_{x^*x^*} + v^*_{y^*y^*} + v^*_{z^*z^*}\right). \qquad \text{[App.9]}$$

The viscosity must also incorporate additional supramolecular turbulence due to the nature of tidal flow (eddy viscosity). These additional turbulence effects are different for vertical and horizontal movement because the horizontal and vertical scales are very different, so horizontal and vertical viscosity parameters are distinguished.

$$u^*_{t^*} + u^*u^*_{x^*} + v^*u^*_{y^*} + w^*u^*_{z^*} = -g^*h^*_{x^*} + A^*_h\left(u^*_{x^*x^*} + u^*_{y^*y^*}\right) + A^*_v u^*_{z^*z^*}, \qquad \text{[App.10]}$$

$$v^*_{t^*} + u^*v^*_{x^*} + v^*v^*_{y^*} + w^*v^*_{z^*} = -g^*h^*_{y^*} + A^*_h\left(v^*_{x^*x^*} + v^*_{y^*y^*}\right) + A^*_v v^*_{z^*z^*}. \qquad \text{[App.11]}$$

Horizontal viscosity is typically small compared to vertical viscosity and other parameters, so the horizontal viscosity terms have a limited contribution. Furthermore the length scale horizontal viscosity operates on is very large while vertical viscosity operates on a limited length scale (water depth). The variation along the horizontal viscosity scale is much smaller than that of the vertical

viscosity scale, the velocity derivatives are small and these terms are therefore dropped from the expressions.

$$u^*_{t^*} + u^* u^*_{x^*} + v^* u^*_{y^*} + w^* u^*_{z^*} = -g^* h^*_{x^*} + A^*_v u^*_{z^* z^*}, \qquad \text{[App.12]}$$

$$v^*_{t^*} + u^* v^*_{x^*} + v^* v^*_{y^*} + w^* v^*_{z^*} = -g^* h^*_{y^*} + A^*_v v^*_{z^* z^*}. \qquad \text{[App.13]}$$

The flow is modelled on the f-plane which leads to the following expressions (including a Coriolis term and a Coriolis parameter which is constant):

$$u^*_{t^*} + u^* u^*_{x^*} + v^* u^*_{y^*} + w^* u^*_{z^*} - f^* v^* = -g^* h^*_{x^*} + A^*_v u^*_{z^* z^*}, \qquad \text{[App.14]}$$

$$v^*_{t^*} + u^* v^*_{x^*} + v^* v^*_{y^*} + w^* v^*_{z^*} + f^* u^* = -g^* h^*_{y^*} + A^*_v v^*_{z^* z^*}. \qquad \text{[App.15]}$$

Expressions [App.1], [App.14] and [App.15] are used as the starting equations in paragraph 2.2.1.

B. RESCALING OF SEVERAL PARAMETERS AND VARIABLES

Some parameters have to be made dimensional again to supply dimensional results in the main text of this thesis. The expressions for these parameters derive from making the governing and derived equations dimensional again.

$$a_q = H^* a_q^* \quad \text{[App.16]}$$

$$a_r = H^* a_r^* \quad \text{[App.17]}$$

$$H_e = H_e^* / H^* \quad \text{[App.18]}$$

$$g = g^* / H^* \quad \text{[App.19]}$$

$$k = k^* / K^* \quad \text{[App.20]}$$

$$k_n = k_n^* / K^* \quad \text{[App.21]}$$

C. THE DEPTH-AVERAGED MODEL

The following expressions to describe depth-averaged tidal flow in an infinite channel are taken from Rienecker & Teubner (1980) and are adjusted to most closely resemble the 3D expressions derived for this research. The expressions presented here are dimensional, as can be seen by the use of asterisks like in the main text of this thesis. The governing equations the expressions for displacement and longitudinal velocity are based on the linear depth-integrated shallow water momentum and mass equations described below:

$$u^*_{t^*} - f^* v^* = -g^* h^*_{x^*} + \frac{r^* u^*}{H^*}, \qquad \text{[App.22]}$$

$$v^*_{t^*} + f^* u^* = -g^* h^*_{y^*} + \frac{r^* v^*}{H^*}. \qquad \text{[App.23]}$$

$$h^*_{t^*} + H^* \left(u^*_{x^*} + v^*_{y^*} \right) = 0. \qquad \text{[App.24]}$$

The following boundary conditions also apply.

$$\int_0^{H^*+h^*} v^* dz^* = 0 \quad \text{at} \qquad y^* = 0, B^* \qquad \text{[App.25]}$$

$$\int_0^{H^*+h^*} u^* dz^* = 0 \quad \text{at} \qquad x^* = 0 \qquad \text{[App.26]}$$

The expressions for η* and u* and the collocation approach referred to in the main text are presented below.

C.I. DISPLACEMENT

The total displacement is calculated as follows.

$$h^* = h_0^* \exp\left(i\left(k_0^* x^* - s^* t^*\right) - a_0^*\left(B^* - y^*\right)\right) + R h_0^* \exp\left(-i\left(k_0^* x^* + s^* t^*\right) - a_0^* y^*\right) + \sum_{n=1}^{N} \frac{h_n^* \exp\left(-i\left(-k_n^* x^* + s^* t^*\right)\right)}{b^* a_n^* - i f^* k_n^*} \left[b^* a_n^* \cos\left(\frac{n p y^*}{B^*}\right) - f^* k_n^* \sin\left(\frac{n p y^*}{B^*}\right) \right], \qquad \text{[App.27]}$$

with the newly introduced parameters:

$$b^* = r_{fr}^* / H^* - i s^* \qquad a_0^* = \frac{-i f^* k_0^*}{b^*} \qquad k_0^* = \sqrt{\frac{i s^* b^*}{g^* H^*}}$$
$$a_n^* = \frac{i n p}{B^*} \qquad k_n^* = \sqrt{a_n^{*2} + k^{*2}} \qquad k^{*2} = \frac{i s^*}{b^* g^* H^*}\left(f^{*2} + b^{*2}\right) \qquad \text{[App.28]}$$

Here r_{fr}* is the only really new parameter; it is the friction parameter in m/s.

C.II. VELOCITY

The total longitudinal velocity is calculated with:

$$U^* = -\frac{g^* a_0^* h_0^*}{f^*}\exp\left(i\left(k_0^* x^* - s^* t^*\right) - a_0^*\left(B^* - y^*\right)\right) + R\frac{g^* a_0^* h_0^*}{f^*}\exp\left(-i\left(k_0^* x^* + s^* t^*\right) - a_0^*\left(B^* - y^*\right)\right) +$$
$$-ig^*\sum_{n=1}^{N}\frac{h_n^* k_n^* a_n^*\exp\left(-i\left(-k_n^* x^* + s^* t^*\right)\right)}{b^* a_n^* - if^* k_n^*}\left[\cos\left(\frac{npy^*}{B^*}\right) - f_n^*\sin\left(\frac{npy^*}{B^*}\right)\right]$$
, [App.29]

with

$$f_n^* = \frac{if^* s^*}{g^* H^* a_n^* k_n^*}. \quad \text{[App.30]}$$

C.II.i VELOCITY FOR COLLOCATION

As for the 3D model in paragraph 4.3 here the expressions to determine the amplitudes of the wave modes are given.

$$R\frac{a_0^*}{f^*}\exp\left(a_0^* y\right) - i\sum_{n=1}^{N}\frac{h_n^* k_n^* a_n^*}{b^* a_n^* - if^* k_n^*}\left[\cos\left(\frac{npy^*}{B^*}\right) - f_n^*\sin\left(\frac{npy^*}{B^*}\right)\right] - \frac{a_0^*}{f^*}\exp\left(a_0^*\left(B^* - y^*\right)\right) = 0$$
[App.31]

at

$$y^* = y_m^* \quad \text{for} \quad m = 1,2,\ldots,N+1 \quad \text{[App.32]}$$

The equivalent in matrix form yields:

$$\begin{bmatrix} A_{K;out}^*\left(y_1^*\right) & A_P^*\left(y_1^*,1\right) & A_P^*\left(y_1^*,2\right) & \mathbb{M} & A_P^*\left(y_1^*,N\right) \\ A_{K;out}^*\left(y_2^*\right) & A_P^*\left(y_2^*,1\right) & A_P^*\left(y_2^*,2\right) & \mathbb{M} & A_P^*\left(y_2^*,N\right) \\ \mathbf{K} & \mathbf{K} & \mathbf{K} & \mathbf{O} & \mathbf{K} \\ A_{K;out}^*\left(y_N^*\right) & A_P^*\left(y_N^*,1\right) & A_P^*\left(y_N^*,2\right) & \mathbb{M} & A_P^*\left(y_N^*,N\right) \\ A_{K;out}^*\left(y_{N+1}^*\right) & A_P^*\left(y_{N+1}^*,1\right) & A_P^*\left(y_{N+1}^*,2\right) & \mathbb{M} & A_P^*\left(y_{N+1}^*,N\right) \end{bmatrix} * \begin{bmatrix} R \\ h_1^* \\ h_2^* \\ \mathbb{M} \\ h_N^* \end{bmatrix} = \begin{bmatrix} -A_{K;in}^*\left(y_1^*\right) \\ -A_{K;in}^*\left(y_2^*\right) \\ \mathbf{L} \\ -A_{K;in}^*\left(y_N^*\right) \\ -A_{K;in}^*\left(y_{N+1}^*\right) \end{bmatrix}, \text{[App.33]}$$

with

$$\left.\begin{aligned} A_{K;in}^* &= -\frac{a_0^*}{f^*}\exp\left(a_0^*\left(B^* - y^*\right)\right) \\ A_{K;out}^* &= \frac{a_0^*}{f^*}\exp\left(a_0^* y\right) \\ A_P^* &= -\frac{ik_n^* a_n^*}{b^* a_n^* - if^* k_n^*}\left[\cos\left(\frac{npy^*}{B^*}\right) - f_n^*\sin\left(\frac{npy^*}{B^*}\right)\right] \end{aligned}\right\}. \quad \text{[App.34]}$$

The amplitude vector is then determined using standard techniques in The Mathworks™ MATLAB®.

D. ELEVATION AMPHIDROMY WITH VARYING VISCOSITY AND SLIP PARAMETERS

In the figure below the elevation amphidromy under influence of changing viscosity parameter can be seen (rate = $A_v^*/A_{v;ref}^*$).

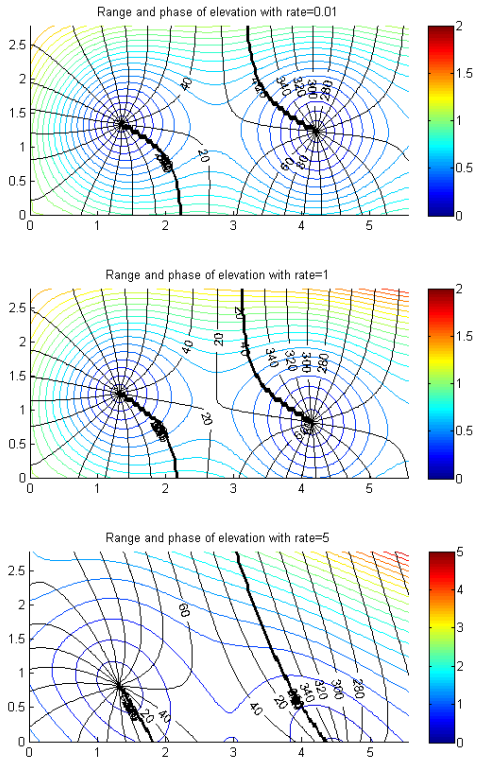

Figure 19: amphidromic system of **η** [m] for varying viscosity

This figure clearly shows a shift of the amphidromic points. This is because dissipation is stronger and therefore the relative influence of the incoming Kelvin wave (as opposed to the outgoing) is stronger along the lateral direction, and the line the amphidromic points lie on rotates towards the lower coast.

In the following figure the elevation amphidromy under influence of changing slip parameter can be seen (rate = s^*/s_{ref}^*).

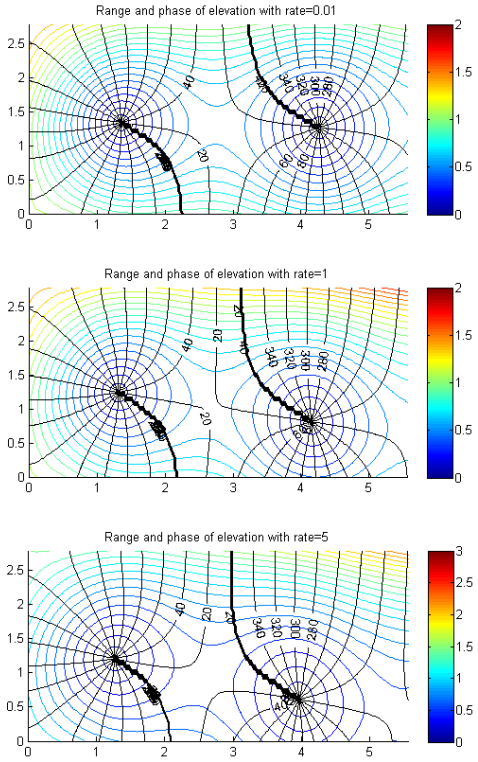

Figure 20: amphidromic system of **η** [m] for varying slip parameter

This figure slows a similar shift of amphidromic points with increasing slip parameter, though the effect is less pronounced than with a changing viscosity parameter. This signifies that the relative magnitude of the viscosity parameter is more important in determining the elevation pattern.

E. AMPLITUDES OF THE KELVIN AND POINCARÉ MODES

For this study five sets of Kelvin and Poincaré modes were used. Their relative amplitudes were derived with a collocation method forced by an incoming Kelvin wave with an amplitude of 1.5 m. The resulting amplitude factors can be found in the table below. Multiplied with the amplitude of the incoming wave the actual amplitude of the respective mode is found.

Mode		3D	2DH			
			Lorentz	**λ***	D*	L_1*
Outgoing Kelvin	R	5.25e-001+ 6.35e-001i	6.37e-001+ 7.07e-001i	6.37e-001+ 6.07e-001i	6.32e-001+ 6.91e-001i	6.63e-001+ 7.49e-001i
Poincaré modes	1	-3.41e-001+ 5.12e-001i	-5.18e-001+ 9.83e-001i	-5.50e-001+ 8.27e-001i	-5.30e-001+ 9.58e-001i	-4.72e-001+ 1.05e+000i
	2	-9.45e-002- 8.69e-002i	-1.99e-001- 1.13e-001i	-1.57e-001- 1.27e-001i	-1.92e-001- 1.17e-001i	-2.16e-001- 9.74e-002i
	3	-8.67e-003+ 2.05e-002i	-1.37e-002+ 4.03e-002i	-5.71e-003+ 4.14e-002i	-1.22e-002+ 4.05e-002i	-1.79e-002+ 3.96e-002i
	4	-1.12e-002- 9.99e-003i	-2.39e-002- 1.26e-002i	-1.97e-002- 1.31e-002i	-2.33e-002- 1.28e-002i	-2.55e-002- 1.15e-002i
	5	-2.21e-003+ 4.89e-003i	-3.33e-003+ 9.74e-003i	-1.35e-003+ 9.83e-003i	-2.97e-003+ 9.78e-003i	-4.32e-003+ 9.60e-003i
	6	-3.40e-003- 3.02e-003i	-7.27e-003- 3.78e-003i	-6.01e-003- 3.86e-003i	-7.08e-003- 3.84e-003i	-7.74e-003- 3.49e-003i
	7	-8.82e-004+ 1.92e-003i	-1.31e-003+ 3.83e-003i	-5.30e-004+ 3.85e-003i	-1.17e-003+ 3.84e-003i	-1.70e-003+ 3.78e-003i
	8	-1.51e-003- 1.34e-003i	-3.23e-003- 1.67e-003i	-2.67e-003- 1.70e-003i	-3.14e-003- 1.70e-003i	-3.44e-003- 1.55e-003i
	9	-4.53e-004+ 9.74e-004i	-6.68e-004+ 1.95e-003i	-2.71e-004+ 1.95e-003i	-5.97e-004+ 1.96e-003i	-8.67e-004+ 1.92e-003i
	10	-8.31e-004- 7.38e-004i	-1.78e-003- 9.21e-004i	-1.47e-003- 9.35e-004i	-1.73e-003- 9.35e-004i	-1.89e-003- 8.53e-004i
	11	-2.73e-004+ 5.84e-004i	-4.01e-004+ 1.17e-003i	-1.63e-004+ 1.17e-003i	-3.59e-004+ 1.17e-003i	-5.21e-004+ 1.16e-003i
	12	-5.28e-004- 4.69e-004i	-1.13e-003- 5.85e-004i	-9.35e-004- 5.93e-004i	-1.10e-003- 5.93e-004i	-1.20e-003- 5.42e-004i
	13	-1.85e-004+ 3.94e-004i	-2.71e-004+ 7.90e-004i	-1.10e-004+ 7.91e-004i	-2.43e-004+ 7.93e-004i	-3.52e-004+ 7.81e-004i
	14	-3.72e-004- 3.31e-004i	-7.97e-004- 4.13e-004i	-6.60e-004- 4.18e-004i	-7.76e-004- 4.19e-004i	-8.48e-004- 3.82e-004i
	15	-1.37e-004+ 2.92e-004i	-2.01e-004+ 5.85e-004i	-8.13e-005+ 5.85e-004i	-1.79e-004+ 5.86e-004i	-2.60e-004+ 5.77e-004i
	16	-2.86e-004- 2.54e-004i	-6.12e-004- 3.17e-004i	-5.07e-004- 3.21e-004i	-5.96e-004- 3.21e-004i	-6.51e-004- 2.93e-004i
	17	-1.09e-004+ 2.32e-004i	-1.60e-004+ 4.66e-004i	-6.47e-005+ 4.66e-004i	-1.43e-004+ 4.67e-004i	-2.07e-004+ 4.60e-004i
	18	-2.36e-004- 2.09e-004i	-5.04e-004- 2.61e-004i	-4.18e-004- 2.64e-004i	-4.91e-004- 2.65e-004i	-5.37e-004- 2.42e-004i
	19	-9.26e-005+ 1.98e-004i	-1.36e-004+ 3.96e-004i	-5.48e-005+ 3.97e-004i	-1.21e-004+ 3.97e-004i	-1.76e-004+ 3.91e-004i
	20	-1.04e-004- 9.20e-005i	-2.22e-004- 1.15e-004i	-1.84e-004- 1.16e-004i	-2.16e-004- 1.16e-004i	-2.36e-004- 1.06e-004i

Figure 21: relative amplitudes of the outgoing Kelvin wave and Poincaré modes for 3D and 2DH (friction parameters based on four different methods)